Journal of Asian Earth Sciences 226 (2022) 105090

Contents lists available at ScienceDirect

Journal of Asian Earth Sciences

journal homepage: www.elsevier.com/locate/jseaes

A late Carboniferous bimodal volcanic suite before closure of the North Tianshan Ocean at the southwestern margin of the Central Asian Orogenic Belt

Wei Xie [a,c,*], Yin Lu [a], Xie-Yan Song [b,*], Yu-Feng Deng [d], Qing-Lin Liang [b], Jun-Nian Yi [e]

[a] Key Laboratory of Marine Hazards Forecasting, Ministry of Natural Resources (MNR), College of Oceanography, Hohai University, Nanjing 210098, China
[b] State Key Laboratory of Ore Deposit Geochemistry, Institute of Geochemistry, Chinese Academy of Sciences, Guiyang 550081, China
[c] Southern Marine Science and Engineering Guangdong Laboratory (Guangzhou), Guangzhou 511458, China
[d] Ore Deposit and Exploration Center (ODEC), Hefei University of Technology, Hefei 230009, China
[e] Institute for Ecological Civilization of Karst Area, Guizhou Normal University, Guiyang 550001, China

ARTICLE INFO

Keywords:
Late Carboniferous
North Tianshan Ocean
Yamansu volcanic arc
Bimodal arc lavas

ABSTRACT

The North Tianshan Ocean (NTO) was one of the youngest oceanic basins at the southwestern margin of the Central Asian Orogenic Belt. When, where and how the NTO was finally consumed and closed have not been well addressed. To better understand the tectonic evolution of the NTO, particularly before its closure, an integrated study of volcanic rocks in the Yamansu volcanic arc has been carried out. Two SHRIMP zircon U–Pb ages (317.6 ± 3.1 Ma and 310.7 ± 2.4 Ma) indicate that the previously identified Permian volcanic rocks erupted during the late Carboniferous instead. The late Carboniferous volcanics in the region are composed of a bimodal suite with a SiO_2 compositional gap between 60 and 70%. The mafic volcanics could be further divided into LREE-poor basalts and LREE-rich basalt-andesites. The LREE-poor variety displays tholeiite and forearc-like characteristics with flat to depleted LREE patterns with $(La/Yb)_N < 1.5$, which were likely derived from a moderately depleted mantle wedge metasomatized by a subducted fluid-like component. The LREE-rich suite is calc-alkaline and has enriched LREE patterns with high $(La/Yb)_N > 2$. They were from a depleted mantle wedge metasomatized by subducted sediment-derived melts, although more or less suffered crustal contamination. The felsic volcanics are I-type rhyolites, derived from anatexis of Cambrian to Mesoproterozoic arc crustal rocks. Here, we suggest that the Kanggur Fault presumably represented the southernmost suture of NTO. The Yamansu volcanic arc was a forearc system of the Central Tianshan continental arc related to southward subduction of the NTO.

1. Introduction

The Central Asian Orogenic Belt (CAOB) is the largest and longest-lived accretionary orogen on Earth (Fig. 1a) and is bounded by the eastern European Craton to the west, the Siberian Craton to the NE, and the North China–Tarim Craton to the south. The CAOB has a long accretionary history of development and mutual interaction of a series of microcontinents, oceanic/continental arcs, seamounts, and accretionary wedges in the immense Paleo-Asian Ocean (Şengör et al., 1993; Windley et al., 2007; Han and Zhao, 2018). The tectonic framework of the CAOB and the geodynamic implications for Phanerozoic continental growth have long been a major focus of studies in the international community. Situated to the north of the Chinese Eastern Tianshan at the southern margin of the CAOB, the North Tianshan Ocean (NTO) was an important branch of the Paleo-Asian Ocean. Particularly, the NTO was one of the youngest oceanic basins during the Paleozoic period and could provide critical constraints on the accretionary history and final amalgamation of the southern part of the CAOB (e.g., Xiao et al., 2004, 2013; Chen et al., 2019; Zhang et al., 2018).

Despite extensive investigations on the accretionary history of the Chinese Eastern Tianshan, the issues of when, where and how the NTO was finally closed to form the Tianshan orogenic system remain hotly debated. It was proposed that the suture zone along the Aqikkuduk Fault was the remnant of the closed NTO and recorded the collision/accretion between the North Tianshan arc system to the north and the Central Tianshan continental arc to the south (e.g., Shu et al., 1999; Xiao et al.,

* Corresponding authors at: Key Laboratory of Marine Hazards Forecasting, Ministry of Natural Resources (MNR), College of Oceanography, Hohai University, Nanjing 210098, China (W. Xie).
E-mail addresses: weixie@hhu.edu.cn, magma_xw@sina.com (W. Xie), songxieyan@vip.gyig.ac.cn (X.-Y. Song).

https://doi.org/10.1016/j.jseaes.2022.105090
Received 20 August 2021; Received in revised form 1 January 2022; Accepted 3 January 2022
Available online 6 January 2022

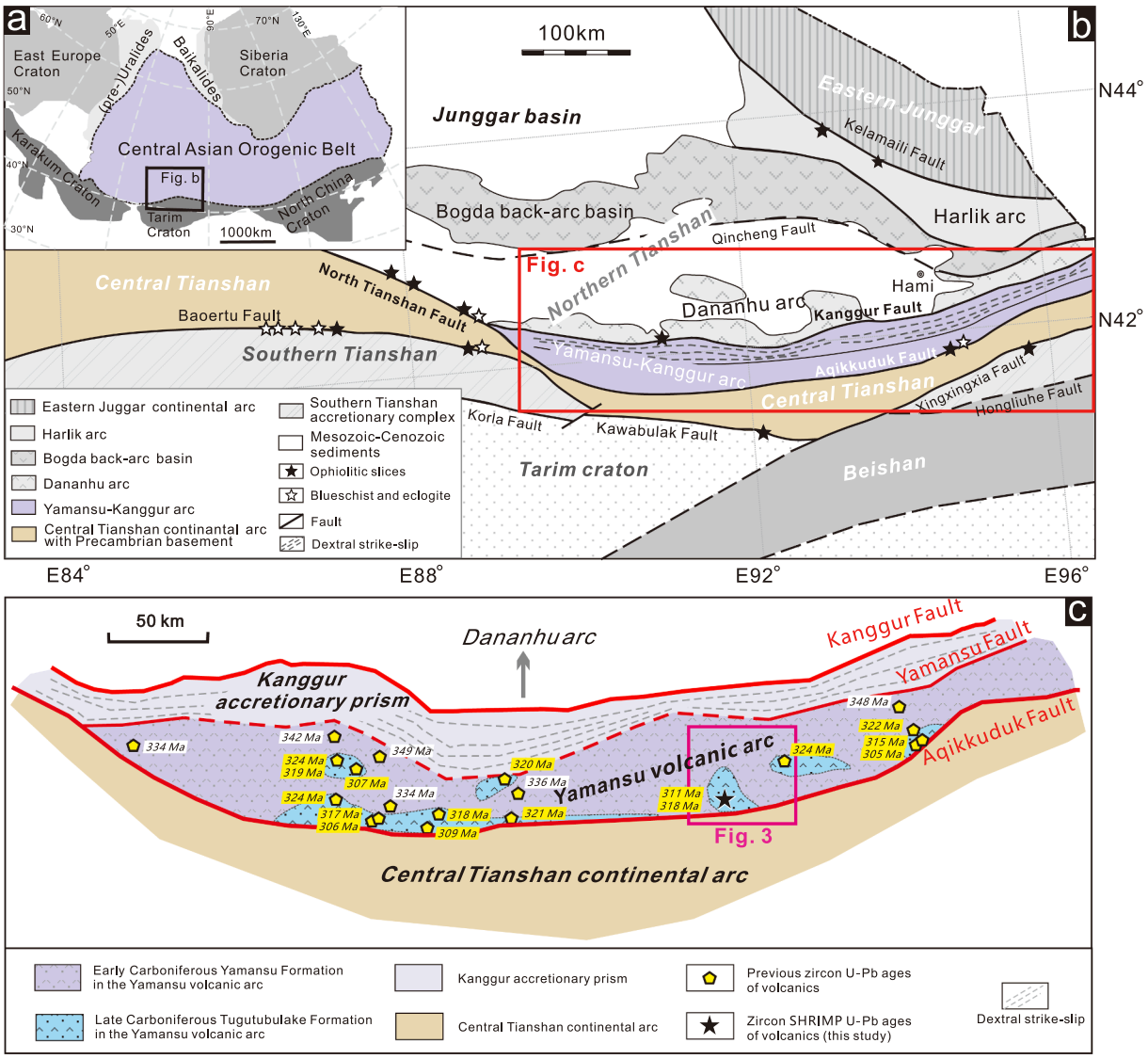

Fig. 1. a) Tectonic outline of the Central Asian Orogenic Belt and surrounding regions (after Şengör et al., 1993; Han and Zhao, 2018). b) Tectonic map of the Eastern Tianshan (modified after Xiao et al., 2004). c) Simplified tectonic map of the Yamansu volcanic arc, Kanggur accretionary prism and Central Tianshan continental arc. Data of zircon U–Pb ages are listed in Table 1.

2004; Zhang et al., 2016b; Han and Zhao, 2018). Alternatively, other authors argued that the Kanggur Fault should be the location of the final closure of the NTO (e.g., Luo et al., 2016; Chen et al., 2019; Zhang et al., 2018). Subsequently, it has still not been addressed that the Yamansu volcanic arc between the Kanggur Fault and the Aqikkuduk Fault belonged to the North Tianshan arc system or the Central Tianshan continental arc. Meanwhile, it is also unclear whether the final closure of the NTO occurred in the early Carboniferous (Xia et al., 2004; Wang and Xu, 2006; Yuan et al., 2007; Zhang et al., 2013) or late Carboniferous-early Permian (Ma et al., 1997; Xiao et al., 2004, 2013; Song et al., 2013; Zhang et al., 2016b; Du et al., 2018; Zhao et al., 2018). Do subduction-related volcanics in the Yamansu volcanic arc still developed during the early Permian? These debates seriously restrict the understanding of the growth mechanism of the Phanerozoic continental crust in the southwestern CAOB.

Compared with the other arcs in the NTO, the Yamansu volcanic arc (Fig. 1, BGMRXUAR, 1993) contains well-preserved Carboniferous-early Permian volcanic-sedimentary strata, while subduction-related volcanic rocks posterior to the Permian were absent in the Eastern Tianshan (Fig. 1). The late Paleozoic volcanic rocks in the Yamansu volcanic arc provide a critical geological record for unraveling regional tectonic history. Thus, in this contribution, we present new SHRIMP U–Pb ages and geochemical data for a suite of late Paleozoic volcanics. Our results suggest that they were a bimodal calc-alkaline arc lava that erupted during the late Carboniferous (318–311 Ma) rather than the early Permian, as suggested by previous studies. Combined with up-to-date data of the late Carboniferous volcanics, we propose that the late Carboniferous bimodal volcanics in the Yamansu volcanic arc were the result of southward subduction of the NTO beneath the forearc setting of the Central Tianshan continental arc at the latest stage.

2. Regional geological background

2.1. General geology of the Tianshan orogenic belt

At the southern margin of the CAOB, the Tianshan Mountains, extending from NW China to Kyrgyzstan and southern Kazakhstan, are subdivided into Western Tianshan and Eastern Tianshan roughly along longitude ~89°E in China (Ma et al., 1997; Xiao et al., 2004, 2013). Eastern Tianshan is separated from the Eastern Junggar terrane to the north by the Kelamaili Suture and from the Tarim craton and Beishan belt to the south by the Kawabulak-Xingxingxia Fault. It is divided into

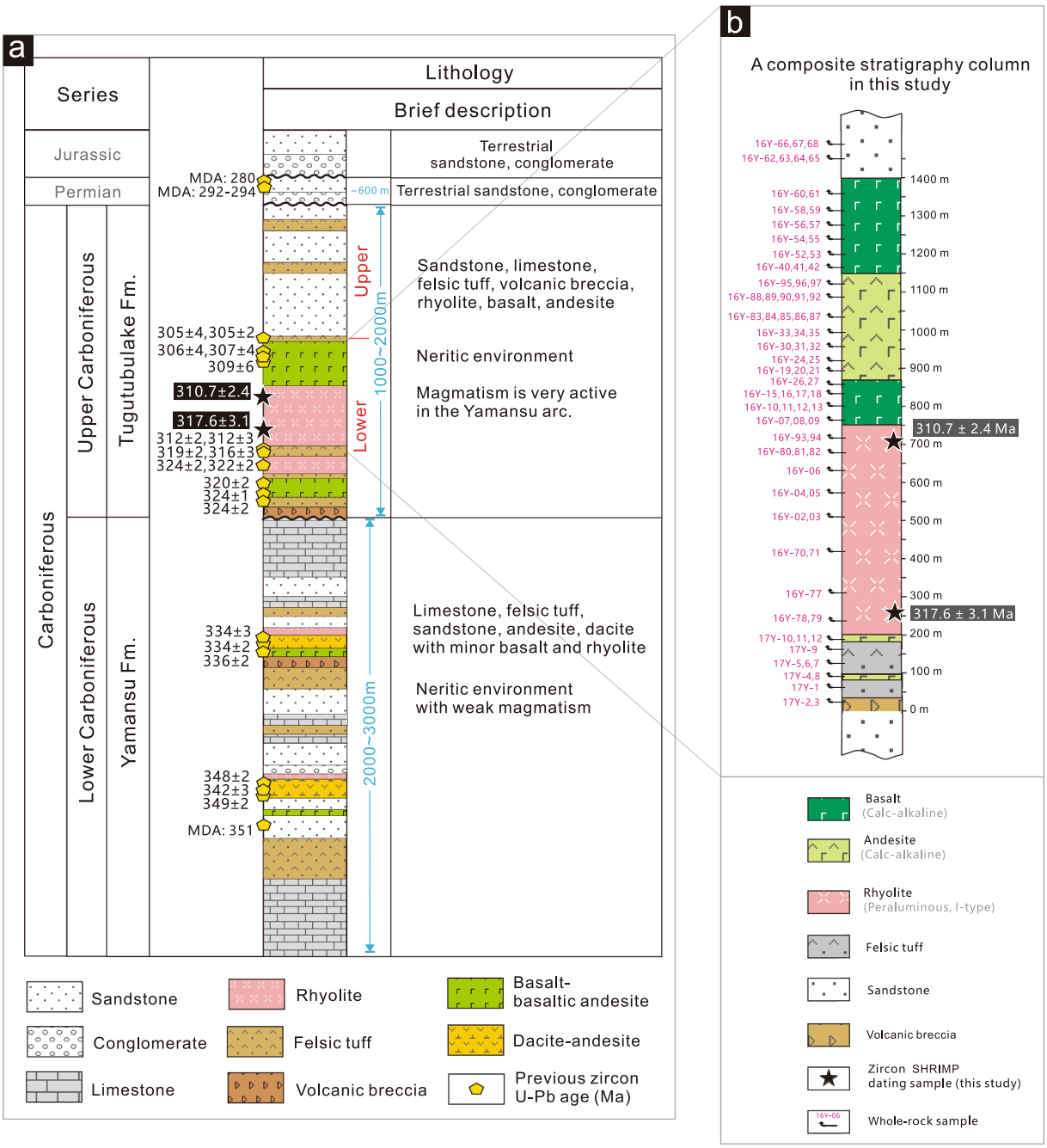

Fig. 2. a) Summarized stratigraphic column for the Yamansu volcanic arc. Blue font means the thickness of strata. MDA is short for the maximum depositional age of sedimentary rocks. Zircon U–Pb ages data are listed in Table 1. b) A composite stratigraphy column in this study, showing the relationship of the different types of volcanic rocks. The location of these volcanic rocks is shown in Fig. 3 below.

the North Tianshan arc system, the Central Tianshan continental margin arc, and the South Tianshan belt from north to south by the Aqikkuduk Fault and the Xingxingxia Fault, respectively (Fig. 1; Xiao et al., 2004; Charvet et al., 2007).

The North Tianshan arc system is predominantly occupied by Paleozoic sedimentary-volcanic strata and magmatic intrusions. Traditionally, it is subdivided into the Harlik-Dananhu arc and Yamansu-Kanggur arc from north to south separated by the Kanggur Fault (Fig. 1b; Xiao et al. 2004; Xie et al., 2016; Han and Zhao, 2018). Xiao et al. (2004) proposed that the Harlik-Dananhu arc was likely formed in the early Ordovician and that a back-arc basin (the Bogda basin) developed in the early Carboniferous. The Yamansu-Kanggur arc consists of the Yamansu volcanic arc and Kanggur accretionary wedge on the two sides of the Yamansu Fault (Fig. 1c; Chen et al., 2019). The Kanggur accretionary wedge is dominantly composed of Devonian-Carboniferous sedimentary rocks with minor volcanic rocks. In contrast, the Yamansu volcanic arc primarily comprises Carboniferous-Permian volcanic-sedimentary rocks that are relatively well preserved but extensively suffer low greenschist facies metamorphism (Xiao et al., 2004; Chen et al., 2019; Song et al., 2021). The Central Tianshan arc is considered a continental arc built on a Precambrian basement that is overlaid by Paleozoic volcanic-sedimentary strata at the southernmost margin of the CAOB (Xiao et al., 2004; Charvet et al., 2007). The main body of the South Tianshan belt consists of Silurian to Carboniferous volcanic-sedimentary strata, which were intensely folded and imbricated by thrusting and faulting (e.g., Xiao et al., 2013).

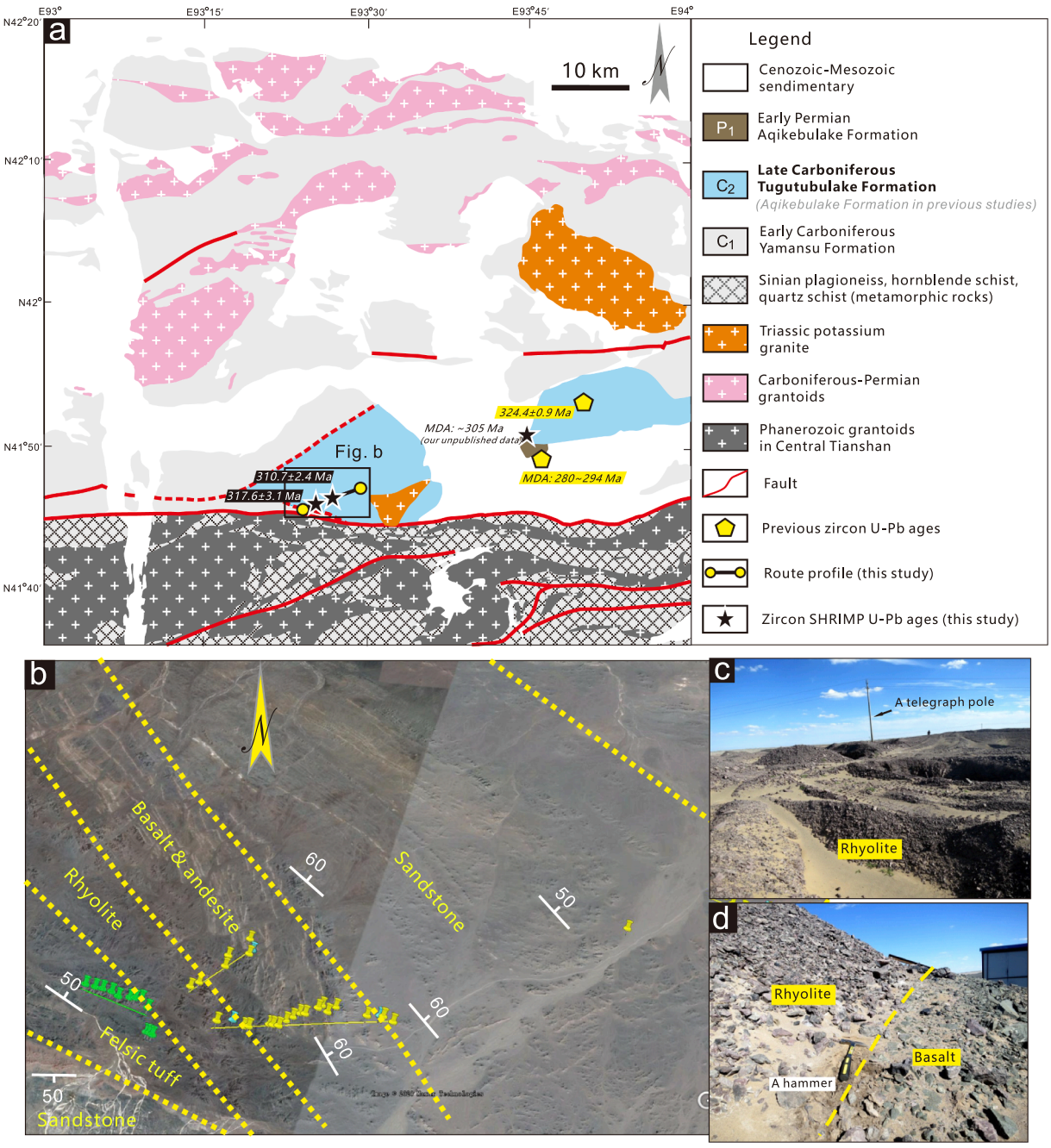

Fig. 3. a) Geological map modified after 1: 200,000 Tuzileike (1976) and Dananhu Geological map 1966. MDA is short for maximum depositional age of sedimentary rocks. Zircon U–Pb ages data are listed in Table 1. b, c, d) Google Earth map and field photos showing the occurrence of volcanic samples.

2.2. Carboniferous-Permian successions in the Yamansu volcanic arc

Generally, in the Yamansu volcanic arc, Carboniferous successions are shallow marine sediments and volcanic rocks, while Permian successions are lacustrine and other terrestrial clastic sediments. Based on abundant rugose corals, fusulines, and some conodonts after large-scale paleontologic surveys and synthetic stratigraphic correlations, reliable stratigraphic ages of the Carboniferous sedimentary units were constrained by Huang et al. (2021). Here, the Carboniferous strata are simply subdivided into two litho-units: early Carboniferous Yamansu Formation and late Carboniferous Tugutubulake Formation (Figs. 1, 2).

The Yamansu Formation is the most widespread strata in the Yamansu volcanic arc (Fig. 1). It is dominantly composed of limestone, sandstone and volcanics with thicknesses of 2000–3000 m (Fig. 2). The limestones are generally interbedded by a few tuffaceous sandstone beds. Carbonate sediments are rich in rugose corals, fusulines and crinoids. Other fossils observed are bryozoans, brachiopods, calcareous algae, foraminifers, and ostracodes (Zhang et al., 2012b; Huang et al., 2021). In addition, one maximum depositional age of a sandstone sample collected from the Yamansu Formation is ca. 351 Ma reported by Chen et al. (2019). The volcanics are identified as two cycles, including dacite, andesite and felsic tuff with minor basalt and rhyolite (Fig. 2). The Tugutubulake Formation, unconformably overlying the Yamansu Formation, is mainly distributed in the Yamansu volcanic arc at 1000–2000 m in thickness. It can be further subdivided into lower and upper units (Fig. 2). The lower unit dominantly consists of basalt-andesite-rhyolite lava, felsic tuff and volcanic breccia, while the upper unit contains sandstone interbedded by thin-bedded tuffs and

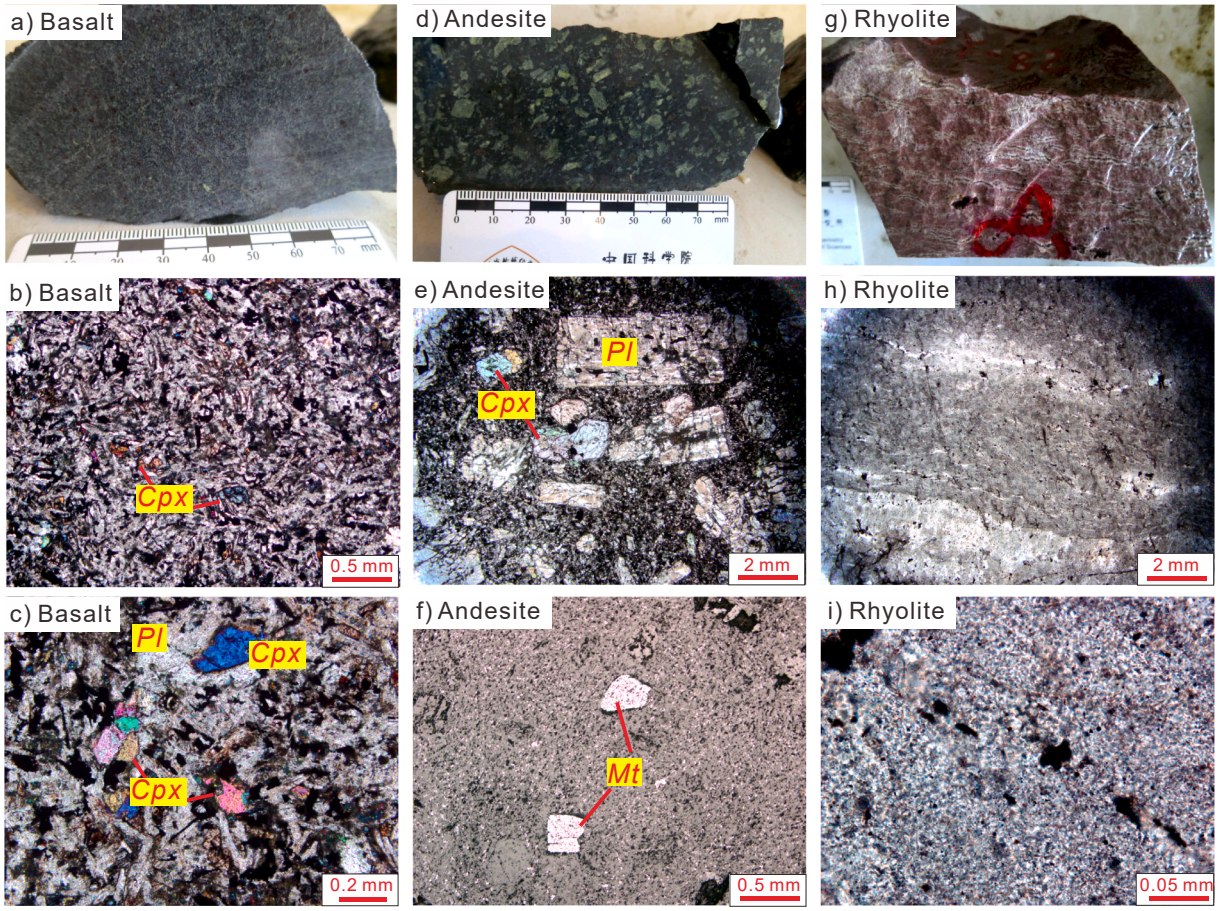

Fig. 4. Hand specimens (a, d, g) and photomicrographs under cross-polarized (b, c, e), plane-polarized (h) and reflected light (f) showing the typical textures of the volcanic rocks in this study. Abbreviations: Cpx = clinopyroxene; Pl = plagioclase; Mt = magnetite.

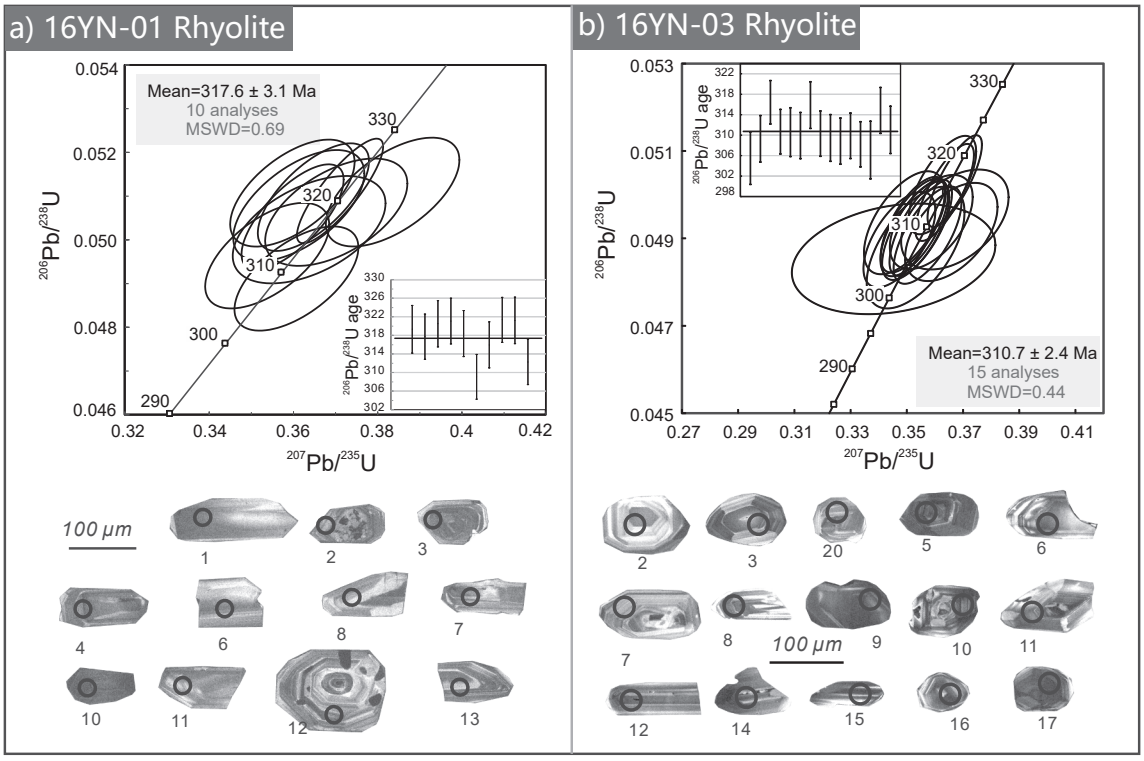

Fig. 5. Concordia plots of SHRIMP zircon U–Pb dating results and CL images of zircons for the studied rhyolites.

limestones.

So far, rare studies have focused on the Permian strata due to their limited and sporadic occurrence in the Yamansu volcanic arc. According to geological surveys during the 1960s and 1970s, the Permian strata are generally subdivided into the Aqikebulake Formation for the lower strata and the Darequanzi Formation for the upper strata. The Darequanzi Formation is composed of lacustrine and other terrestrial sandstone and conglomerate, whereas the Aqikebulake Formation dominantly contains basalt-andesite-rhyolite lava, felsic tuff and volcanic breccia with some marine fossils (BGMRXUAR, 1993). However, no radiometric ages have been dated yet. One well-preserved volcanic strata of the Aqikebulake Formation is studied below in this contribution (Fig. 3).

Integrating the field data, a comprehensive composite stratigraphy column is set up. As shown in Fig. 2b, it consists of felsic tuff, rhyolite, and basalt with an interlayer of andesite from bottom to top. These layers are conformably in contact with each other (Fig. 3). Basalts display dark green and aphyric texture without vesicular or amygdaloidal structures, and the matrix contains tiny plagioclase and clinopyroxene with minor Fe-Ti oxides and secondary carbonates. Plagioclase crystals are slightly to moderately altered to sericite, while clinopyroxene is commonly partially altered to chlorite and secondary magnetite (Fig. 4a, b, c). In contrast, green andesites including basaltic andesites show a porphyritic texture with 10–20 vol% phenocrysts. The phenocrysts are mainly plagioclase and clinopyroxene with minor finer-grained magnetite. The groundmass is mainly composed of plagioclase, clinopyroxene, and Fe-Ti oxides. The phenocrysts are slightly altered while the groundmass is altered to chlorite, sericite, secondary magnetite and secondary carbonates (Fig. 4d, e, f). Rhyolites are purple and aphyric without quartz or feldspar phenocryst (Fig. 4g, h, i). The groundmass is mainly composed of aphanitic feldspar and quartz, and minor amounts of opaque minerals, showing rhyolitic structure.

3. Analytical methods

3.1. Zircon U–Pb dating

Approximately 3 kg of each rhyolite (16YN-01 and 16YN-03) was crushed for zircon crystal separation (Fig. 2b). More than 300 zircon grains were obtained from each sample. Cathodoluminescence (CL) images (Fig. 5) were obtained on a Hitachi S3000N scanning electron microscope (SEM) at the Beijing SHRIMP Centre. U–Pb dating analyses were undertaken on a SHRIMP II at the Beijing SHRIMP Centre (National Science and Technology Infrastructure), following the analytical protocols of Compston et al. (1992) and Williams (1998). Zircon standard SL 13 was measured to calibrate U, Th and Pb concentrations. Zircon standard TEMORA-2 (416.8 Ma, Black et al., 2004) was used for isotopic fractionation correction. The ^{204}Pb-based method by Stacey and Kramers (1975) was used for common Pb correction. The data were processed using the SQUID 1.02 and Isoplot 3.0 programs of Ludwig (2001, 2003). Uncertainties for each analysis are expressed as 1σ. The weighted mean age is quoted as 2σ. Calculated mean ages are presented at 95% confidence. 2 s error of mean in standard TEMORA-2 calibration: ±0.74% for 16YN-01, ±0.8% for 16YN-03 should be included in error propagation as required when comparing data from different mounts/sessions.

3.2. Whole-rock major, trace elements and Sr-Nd isotopes

Approximately seventy relatively fresh samples (Fig. 2b) were chosen for the whole-rock geochemical analysis. Major oxides were measured using a PANalytical Axios X-ray fluorescence spectrometer (XRF) on fused glass beads at ALS Chemex (Guangzhou) Co Ltd. with an analytical uncertainty of less than 5%. 0.7 g powder of these samples was mixed completely with $Li_2B_4O_7$ and then fused to a glass bead at 1050–1100 °C in an automatic melting instrument. Trace element concentrations were determined using a Perkin-Elmer Sciex ELAN DRC-e

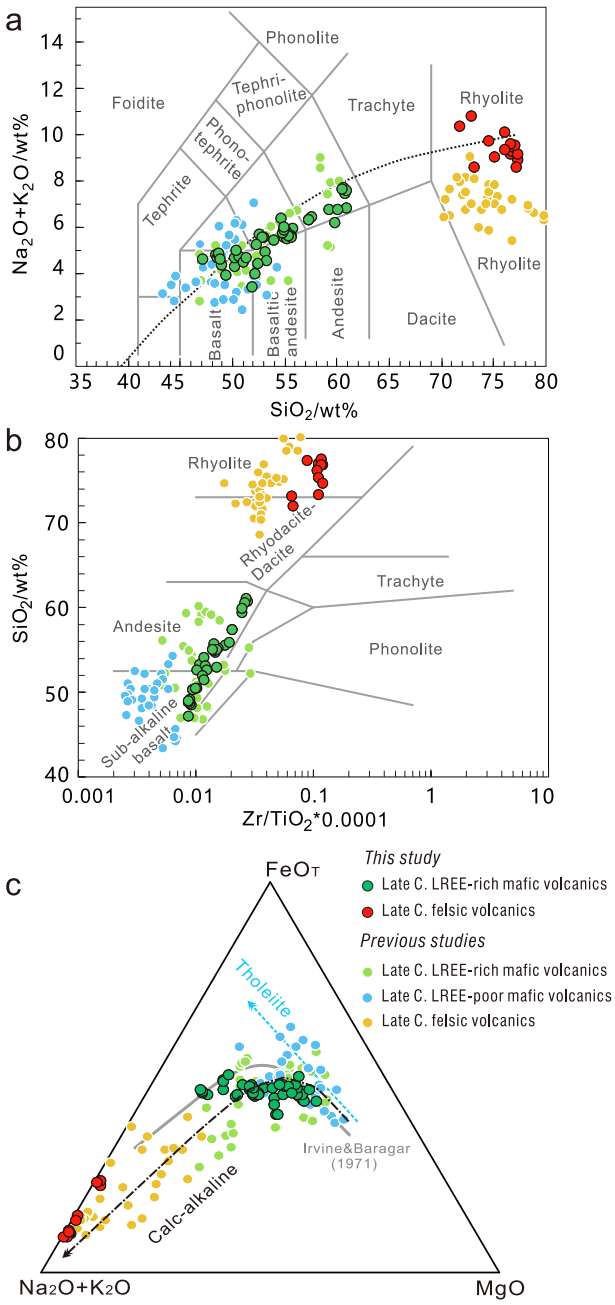

Fig. 6. (a) Plot of total alkalis versus SiO_2 (reference lines after Le Maitre, 1989); (b) plot of SiO_2 versus Zr/TiO_2 (reference lines after Winchester and Floyd, 1977); (c) total alkalis–FeO_T–MgO discrimination diagram (Irvine and Baragar, 1971). Previous whole-rock data sources of the late C. (Carboniferous) volcanics are listed in Appendix S3.

inductively coupled plasma mass spectrometer (ICP–MS) at the State Key Laboratory of Ore Deposit Geochemistry, the Institute of Geochemistry, Chinese Academy of Sciences. The USGS and Chinese National standards AGV-2, BHVO-2, GSR-1, GSR-2, GSR-3 and W-2 were chosen to calibrate the element concentrations of the analysed samples. The analytical precision is better than 5% for elements > 10 ppm and less than 8% for those < 10 ppm. The procedure for the trace elements is described in detail by Qi et al. (2000).

Whole rock Sr and Nd isotopic ratios were measured with a Micromass Isoprobe Multi-Collector ICP–MS at State Key Laboratory of Isotope Geochemistry, Guangzhou Institute of Geochemistry, Chinese Academy of Sciences, using analytical procedures described by Li et al.

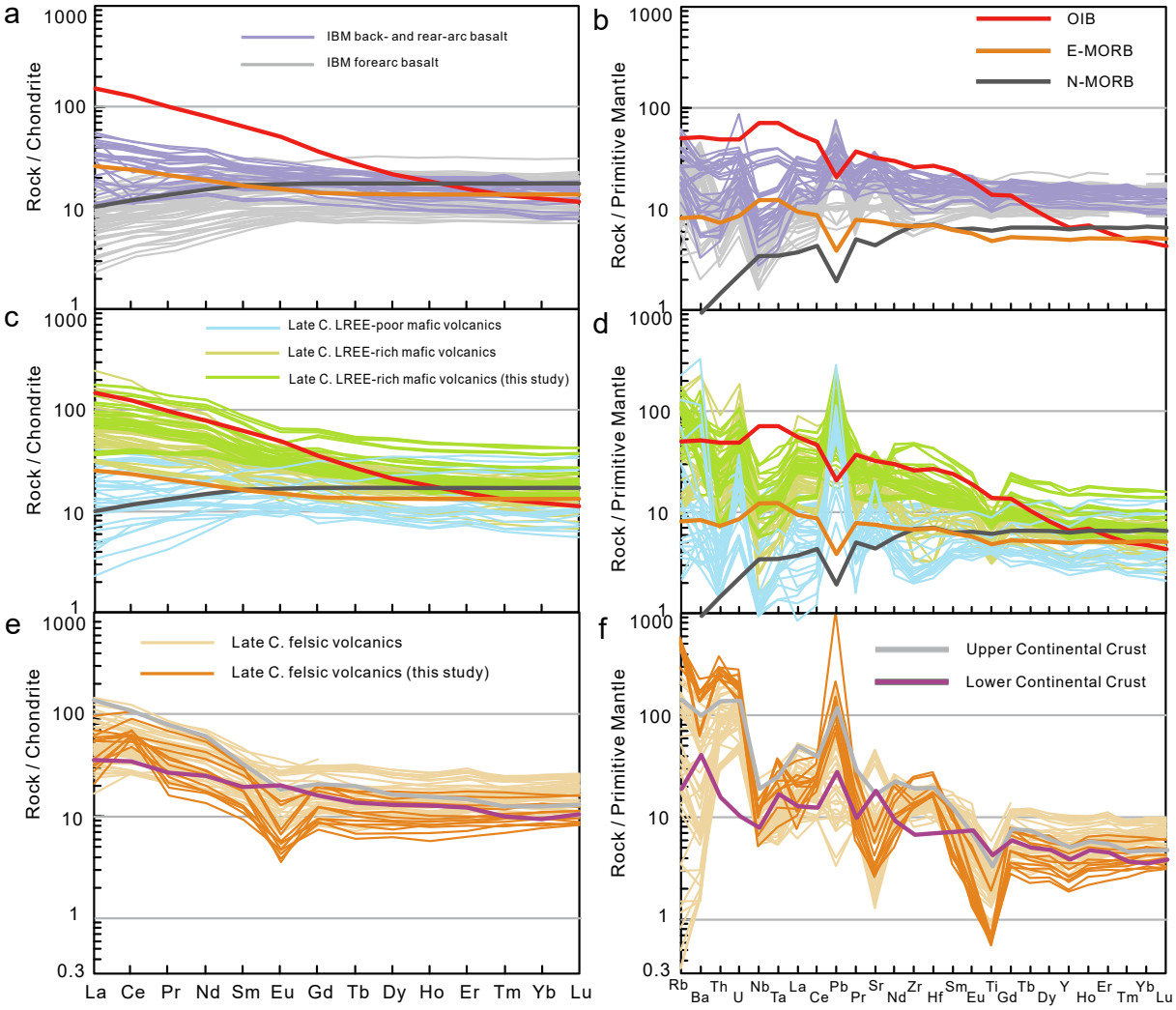

Fig. 7. (a, c, e) Chondrite-normalized REE diagrams and (b, d, f) primitive mantle-normalized multi-element variation diagrams for late C. (Carboniferous) volcanics in the Yamansu volcanic arc. Normalizing values, N-MORB, E-MORB and OIB are cited from McDonough and Sun (1995). Values of the upper continental crust (UCC) and lower continental crust (LCC) are from Rudnick and Gao (2003). Izu-Bonin-Mariana (IBM) back- and rear-arc basalt: Ishizuka et al. (2009), Izu-Bonin-Mariana (IBM) forearc basalt: Taylor and Nesbitt (1998), Tamura et al. (2005), and Reagan et al. (2010). Previous whole-rock data sources of the late C. volcanics are listed in Appendix S3.

(2006). The mass fractionation corrections for the isotopic ratios are based on $^{86}Sr/^{88}Sr = 0.1194$ and $^{146}Nd/^{144}Nd = 0.7219$. The reported $^{86}Sr/^{88}Sr$, and $^{143}Nd/^{144}Nd$ ratios were adjusted to the NBS SRM 987 standard $^{87}Sr/^{86}Sr = 0.71025$ and the Shin Etsu JNdi-1 standard $^{143}Nd/^{144}Nd = 0.512115$, respectively.

4. Analytical results

4.1. Zircon U–Pb ages

Zircon grains separated from the rhyolite samples (16YN-01, 16YN-03) are mostly transparent and colorless. They are subhedral to euhedral and show oscillatory zoning texture, with a few of them containing unknown inclusions (Fig. 5). In this study, 32 analysed spots at the margins of zircons were carried out (Table 2). The results display large variations in U and Th concentrations (171–1516 ppm and 90–1072 ppm, respectively) with magmatic-type Th/U ratios of 0.5–1.2. In the age-dating zircons, only seven inherited zircons (327–483 Ma of apparent $^{206}Pb/^{238}U$ ages; Table 2) are found in the Concordia plots *(not shown here)*. The remaining twenty-five analyses form a tight cluster on the Concordia plots and yield weighted mean $^{206}Pb/^{238}U$ ages of 317.6 ± 3.1 Ma (16YN-01) and 310.7 ± 2.4 Ma (16YN-03), respectively (Fig. 5). Considering the systematic error of different mounts/sessions at the same SHRIMP instrument, the two ages are consistent with each other. They suggest that the volcanic suite was formed during the late Carboniferous (318–311 Ma).

4.2. Whole-rock major, trace elements and Sr-Nd isotopic compositions

The whole-rock data of the volcanics in this study are listed in Appendices S1 and S2, respectively. The basalts and andesites have high LOI (loss on ignition) contents ranging from 1.0 to 5.7%, consistent with petrographic evidence for partial alteration. In contrast, the rhyolites have low LOI contents of −0.2 to 0.9%. In the following plots and discussion, all oxide contents of the samples were recalculated to 100% on a volatile-free basis with all Fe as FeO_T.

As Na_2O and K_2O might mobilize during alteration, the Zr/TiO_2 versus SiO_2 diagram (Winchester and Floyd, 1977) is also utilized for rock classification here, because Zr and Ti are considered to remain immobile during alteration/weathering. The samples have a compositional gap in the plots of SiO_2 versus $Na_2O + K_2O$ and Zr/TiO_2 versus SiO_2, suggesting a bimodal volcanic suite (Fig. 6a and b). The mafic

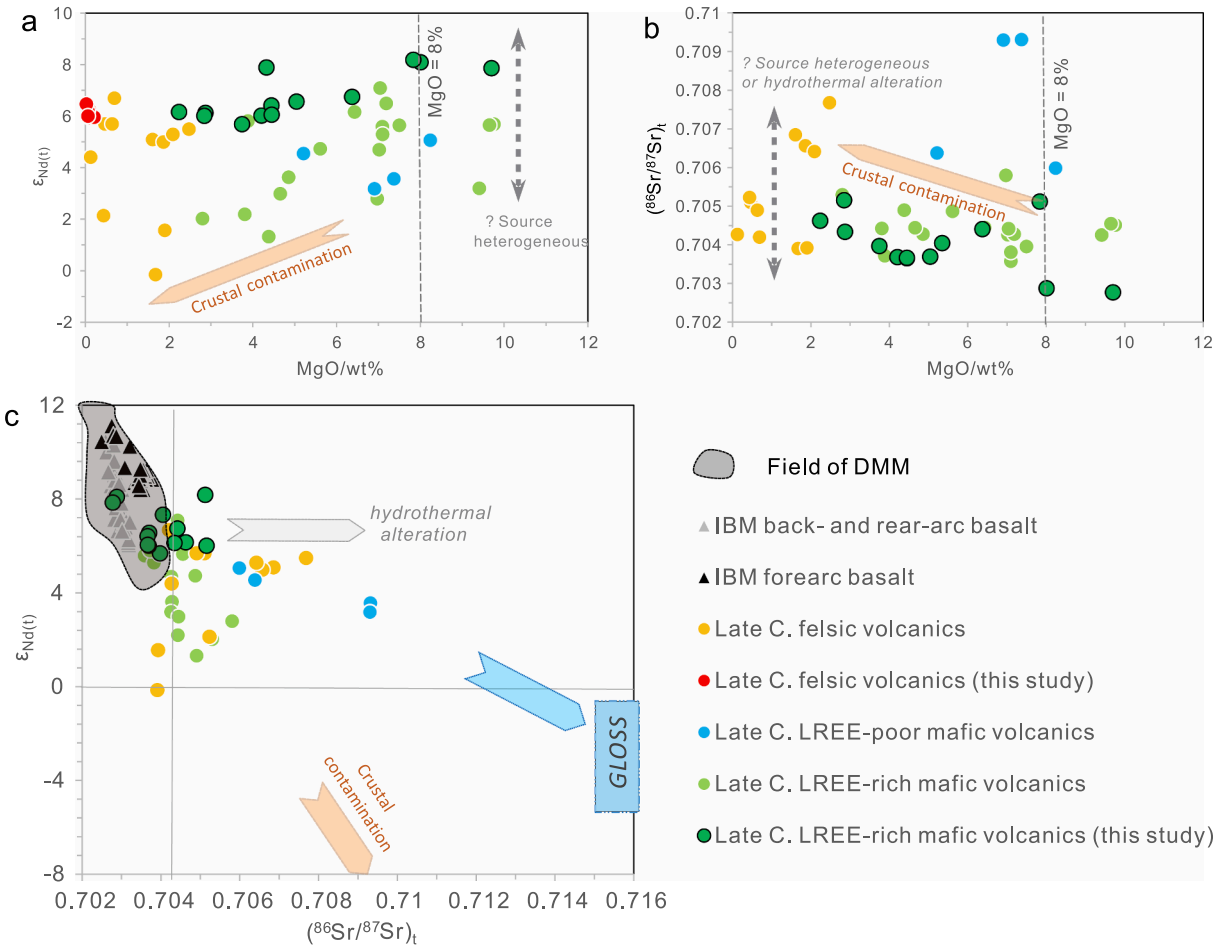

Fig. 8. (a, b) plots of $\varepsilon_{Nd}(t)$, $(^{86}Sr/^{87}Sr)_t$ versus MgO; (c) $\varepsilon_{Nd}(t)$ vs. $(^{86}Sr/^{87}Sr)_t$ diagram. Data for the fields of DMM (depleted MORB mantle) and GLOSS (global subducting sediments) are cited from Stracke (2012) and Plank and Langmuir (1998), respectively. Other data source is the same as in Fig. 7.

samples (basalts and andesites) show scattered SiO_2 (47.2–61.2%) and cross the basaltic andesite field, belonging to the calc-alkaline series (Fig. 6). They display chondrite-normalized REE patterns slightly enriched in LREEs with $(La/Yb)_N$ ranging from 2.2 to 6.6, and slightly positive to negative Eu anomalies with Eu/Eu* from 1.1 to 0.86 (Fig. 7c). Furthermore, they have primitive mantle-normalized trace element patterns enriched in large ion lithophile elements (LILEs) relative to high field strength elements (HFSEs) and show negative Nb (-Ta) and Ti anomalies, and positive Pb anomalies (Fig. 7d). Compared with the basalts, the andesites contain higher Th and scattered Zr-Hf contents, some of which show pronounced positive Zr-Hf anomalies. Here, fourteen basalts and andesites with low Rb/Sr ratios (0.04–0.3) were selected for Sr-Nd isotope analysis to minimize post-magmatic hydrothermal alteration. As shown in Fig. 8, the basalts and andesites have low initial $(^{86}Sr/^{88}Sr)_t$ values of 0.7028–0.7052 and high $(^{143}Nd/^{144}Nd)_t$ values of 0.5125–0.5127 ($\varepsilon_{Nd(t)} = +5.69 - +8.20$).

The rhyolites have 71.8 to 77.4% SiO_2, A/CNK [molar ratio of $Al_2O_3/(CaO + Na_2O + K_2O)$] from 0.99 to 1.1 (except one sample is 1.23) and A/NK [molar ratio of $Al_2O_3/(Na_2O + K_2O)$] from 1.05 to 1.2, similar to slightly peraluminous silicic rocks *(not shown here)*. They show chondrite-normalized REE patterns enriched in LREEs with $(La/Yb)_N$ of 2.7 to 7.4, significantly negative Eu anomalies with Eu/Eu* from 0.24 to 0.65 and positive Ce anomalies with Ce/Ce* from 1.0 to 3.2 (Fig. 7e). They are very rich in LILEs and have primitive mantle-normalized trace element patterns with negative Nb (-Ta), Eu and Ti anomalies, positive Pb and Zr-Hf anomalies (Fig. 7f). All rhyolite samples have very high Rb/Sr ratios varying from 1.9 to 5.8, indicating that their mobile Rb element was likely affected by post-magmatic hydrothermal alteration. Thus, Nd isotopes were just analysed here. Rhyolites have relatively restricted initial $(^{143}Nd/^{144}Nd)_t$ from 0.51254 to 0.51257 and $\varepsilon_{Nd(t)}$ from + 5.96 to + 6.47 (Fig. 8a). Because they have similar continental crustal $^{147}Sm/^{144}Nd$ ($f_{Sm/Nd} = -0.48$ to -0.28), the calculated one-stage Nd model ages are selected here, which range from 553 to 685 Ma.

5. Discussion

5.1. Effusive ages of the volcanics in the Yamansu volcanic arc

Based on abundant index fossils, the Yamansu and Tugutubulake Formations in the Yamansu volcanic arc were formed during the early and late Carboniferous, respectively (e.g., Zhang et al., 2012b; Huang et al., 2021). Nevertheless, the Permian Aqikebulake and Darequanzi Formations have rare reliable stratigraphic and radiometric ages. The two zircon U–Pb ages of 317.6 ± 3.1 Ma and 310.7 ± 2.4 Ma obtained by SHRIMP analyses (Fig. 5) for the rhyolites in this study strongly suggest that the volcanics from the Aqikebulake Formation erupted during the late Carboniferous rather than the early Permian. Additionally, it is strikingly noting that the volcanic sequence of the Aqikebulake Formation is very similar to the lower unit of the Tugutubulake Formation as aforementioned (Fig. 2). Thus, they could be incorporated into the Tugutubulake Formation.

A few zircon U–Pb ages indicate that the early Carboniferous volcanics have two short magmatic episodes (342–349 Ma and ~ 335 Ma) in the Yamansu volcanic arc (Table 1). In contrast, nearly twenty precise zircon U–Pb ages for the late Carboniferous volcanics arc have been published, displaying a relatively long effusive period (325–305 Ma).

Table 1
Summary of zircon U–Pb ages of the late Paleozoic volcanic rocks and sedimentary rocks in the Yamansu volcanic arc.

Number	Location	Dating sample	Ages (Ma)	Dating method	References
Mafic and felsic volcanic rocks					
Tugutubulake Formation					
1	Yamansu	Rhyolite	310.7 ± 2.4	SHRIMP	This study
2	Yamansu	Rhyolite	317.6 ± 3.1	SHRIMP	
3	Yamansu	Basalt	324.4 ± 0.9	LA-ICP-MS	Hou et al., 2014
4	Jueluotage	Basaltic andesite	320 ± 2	LA-ICP-MS	Luo et al., 2016
5	Jueluotage	Basaltic andesite	321 ± 2	LA-ICP-MS	
6	Jueluotage	Rhyolite	320 ± 1.2	LA-ICP-MS	Li et al., 2011
7	Shaquanzi	Andesite	314.7 ± 3	LA-ICP-MS	Jiang et al., 2017
8	Shaquanzi	andesitic tuff	305.3 ± 3.5	LA-ICP-MS	
9	Shaquanzi	Rhyolite	321.7 ± 1.7	LA-ICP-MS	Xu et al., 2014
10	Shaquanzi	Diorite porphyry	322.2 ± 1.7	LA-ICP-MS	
11	Aqishan	Rhyolite	324.4 ± 1.5	LA-ICP-MS	Cui et al., 2018
12	Aqishan	Andesite	318.6 ± 1.4	LA-ICP-MS	
13	Bailingshan	Tuffaceous dacite	324.1 ± 2.1	LA-ICP-MS	Zhang et al., 2016a
14	Shilipo	Basalt	307 ± 4	LA-ICP-MS	Yuan et al., 2007
15	Heijianshan	Basalt	306.2 ± 4.0	SHRIMP	Zhang et al., 2012a,
16	Dongjianfeng	Basalt	308.9 ± 5.8	LA-ICP-MS	**2013
17	Heijianshan	Rhyolite tuff	315.6 ± 2.6	LA-ICP-MS	Zhao et al., 2018
18	Shuanglong	Andesite tuff	319.1 ± 1.9	LA-ICP-MS	Zhang et al., 2020
19	Shuanglong	Andesite tuff	312.0 ± 1.7	LA-ICP-MS	
20	Shuanglong	Rhyolite tuff	312.4 ± 2.5	LA-ICP-MS	
21	Shuanglong	Andesite tuff	305.4 ± 1.6	LA-ICP-MS	
Yamansu Formation					
22	Shaquanzi	Dacite	348.0 ± 1.7	LA-ICP-MS	Luo et al., 2012,
23	Jiabaishan	Basaltic andesite	336 ± 2	LA-ICP-MS	**2016
24	Jiabaishan	Dacite	335.9 ± 2.4	LA-ICP-MS	
25	Chilongfeng	Rhyolite	334.0 ± 2.5	LA-ICP-MS	
26	Shuanglong	Rhyolite	341.0 ± 1.9	LA-ICP-MS	Zhang et al., 2020
27	Shuanglong	Rhyolite tuff	333.2 ± 2.0	LA-ICP-MS	
28	Hongshanliang	Rhyolite	348.8 ± 2.1	LA-ICP-MS	Zhao et al., 2019
29	Aqishan	Rhyolite	341.7 ± 2.7	LA-ICP-MS	Su et al., 2009
Sedimentary rocks (Maximum depositional age, MDA)					
Yamansu Formation					
1	Yamansubei	Greywacke	351	LA-ICP-MS	Chen et al., 2019
Aqikebulake Formation					
2	Yamansu	Sandstone	280	LA-ICP-MS	Zhang et al., 2016b
3	Yamansu	Sandstone	292	LA-ICP-MS	
4	Yamansu	Sandstone	294	LA-ICP-MS	

The two new zircon SHRIMP U–Pb ages in this study fall well within the late Carboniferous effusive period (325–305 Ma) constrained by previous studies. As shown in Fig. 1c, the late Carboniferous volcanics are widely distributed throughout the Yamansu volcanic arc. They are dominantly composed of bimodal suites (a SiO_2 compositional gap between 60 and 70%; Fig. 6). To reveal the nature of magmatism during the latest stage before closure of the NTO, petrogenesis of the late Carboniferous bimodal volcanics will be discussed in detail below.

As the late Carboniferous bimodal lavas suffered low greenschist facies metamorphism, the effect of hydrothermal alteration on the geochemistry cannot be ignored given their relatively high LOI (up to 5.7%). The lack of correlation between Rb, Ba, K, Sr, Pb and Zr indicates that these large ion lithophile elements were mobile during post-magmatic alteration. In contrast, REEs, Nb, Hf, and Th show positive correlations with Zr, suggesting that these elements remained essentially immobile during surface processes *(not shown here)*. Although the late Carboniferous samples have varied U contents, most of them also show positive correlations with Zr under U < 2 ppm (Fig. 9a). Hence, in the following discussion, we mainly focus on the abundances and ratios of U and immobile elements. For Sr-Nd isotopes, samples with low Rb/Sr ratios (<0.3) were selected to minimize post-magmatic hydrothermal alteration.

5.2. Petrogenesis of the mafic volcanics

According to the light rare earth element (LREE) contents, the mafic volcanics from the lower Tugutubulake Formation could be subdivided into LREE-poor and LREE-rich varieties. The LREE-poor samples are tholeiite basalts (Fig. 6) and have low LREE/HREE ratios most of which display $(La/Yb)_N < 1.5$, showing N-MORB-like flat to depleted LREE patterns in Fig. 7c. The LREE-rich rocks are calc-alkaline basalts and andesites with high LREE/HREE ratios, for instance $(La/Yb)_N > 2$, including the analysed volcanics in this study.

The LREE-poor mafic volcanics are characterized by strong enrichment in LILEs and strong depletion in Th, Nb-Ta and Zr-Hf, akin to the Izu-Bonin-Mariana (IBM) forearc basalt (Fig. 7). Their low Nb/Yb (0.38–2.8) and Th/Yb (0.06–0.28) ratios are also close to the IBM forearc basalt (Fig. 9c). The features of trace elements infer that the LREE-poor suites were attributed to the addition of subducted inputs rather than crustal contamination because crustal rocks are typically characterized by enrichments in LREEs, Th and Zr-Hf. Generally, for modern arc basalt, highly mobile elements (e.g., Rb, Sr, Ba, U) are concentrated into aqueous slab-derived fluids, whereas Th and LREEs are partitioned into sediment-derived melts (e.g., Elliott et al., 1997; Hawkesworth et al., 1997; Singer et al., 2007). Most of the LREE-poor suites have high U/Th (up to 6.2), pointing to the effect of aqueous slab-derived fluids in the source (Fig. 9d). Moreover, the Nd isotopic ratios of the LREE-poor suites ($\varepsilon_{Nd(t)} = +3.2$ to $+5.1$) are more enriched than those of the IBM forearc basalt (Fig. 8c). Hence, they were derived from a moderately depleted mantle wedge which had been metasomatized by subducted fluid-like component (Fig. 9).

The calc-alkaline LREE-rich basalts and andesites have similar REE and trace element patterns (Fig. 7) and Sr-Nd isotopic values (Fig. 8), implying that they should be derived from the same primitive magmas and mantle source. They are characterized by "arc-like" trace elements with strong enrichment in LILEs with negative Nb (-Ta) and Ti anomalies, positive Pb anomalies, but by relatively high HFSEs, such as REE, Th and Zr-Hf concentrations (Fig. 7d). These geochemical signatures can be attributed to crustal contamination during the ascent of magmas or reflect that of mantle sources. There are a few lines of evidence for crustal contamination: a) both $\varepsilon_{Nd(t)}$ and $(^{86}Sr/^{88}Sr)_t$ display trends of crustal contamination when plotted against MgO (Fig. 8a, b); b) the andesites have scattered Zr-Hf contents, some of which show pronounced positive Zr-Hf anomalies (Fig. 7d). Nevertheless, some LREE-rich basalts contain MgO > 8% and $Mg^{\#}$ of 0.58–0.65, showing aphyric texture without any phenocrysts (Fig. 4). They could be considered

Table 2
SHRIMP U–Pb isotopic data for zircons of the rhyolites in the Yamansu volcanic arc.

Spot	^{206}Pb[a]	^{206}Pb[b]	U	Th	$^{207}Pb/^{206}Pb$	±%	$^{207}Pb/^{235}U$	±%	$^{206}Pb/^{238}U$	±%	Apparent ages (Ma)					
	ppm	%	ppm	ppm							$^{206}Pb/^{238}U$	±1σ	$^{207}Pb/^{206}Pb$	±1σ	$^{208}Pb/^{232}Th$	±1σ
16YN-01 Rhyolite																
01-1	12.0	0.00	275	154	0.05159	2.3	0.3613	2.8	0.05079	1.6	319.3	5.1	267.4	53	323.0	7.8
01-2	30.9	0.05	712	591	0.05165	1.6	0.3598	2.2	0.05052	1.6	317.7	4.9	269.9	36	306.1	5.7
01-3	22.4	0.29	509	269	0.05189	1.8	0.3647	2.4	0.05098	1.6	320.5	5.0	280.7	41	315.6	6.7
01-4	30.4	0.20	690	398	0.05109	2.2	0.3598	2.7	0.05107	1.6	321.1	4.9	244.9	51	301.5	6.9
01-5	23.9	0.14	531	403	0.05388	1.6	0.3882	2.3	0.05225	1.6	328.3	5.1	366.2	37	325.4	6.3
01-6	20.7	0.27	474	300	0.05302	2.5	0.3702	3.0	0.05063	1.6	318.4	5.0	329.7	58	297.5	7.3
01-7	20.0	0.00	476	357	0.05326	2.2	0.3607	2.7	0.04912	1.6	309.1	4.8	339.9	49	306.6	6.6
01-9	45.8	0.25	1001	1072	0.05414	1.7	0.3965	2.3	0.05312	1.6	333.6	5.1	377.1	39	332.9	5.9
01-10	17.5	0.37	403	265	0.05251	2.9	0.3637	3.3	0.05023	1.6	316.0	5.0	307.9	65	304.1	7.7
01-11	65.0	0.00	1479	787	0.05265	1.0	0.3711	1.8	0.05112	1.5	321.4	4.8	313.6	22	313.9	5.9
01-12	17.8	0.00	407	313	0.05444	2.2	0.3836	2.7	0.05109	1.6	321.2	5.0	389.5	49	325.5	7.0
01-13	17.7	0.28	413	361	0.05169	2.2	0.3538	2.7	0.04964	1.6	312.3	4.9	271.7	51	305.2	9.1
01-14	23.3	0.16	515	337	0.05260	2.3	0.3818	2.8	0.05265	1.6	330.7	5.1	311.8	53	313.7	8.7
01-15	67.8	0.03	1516	748	0.05233	1.3	0.3755	2.0	0.05204	1.5	327.0	4.9	300.1	29	319.0	6.0
01-16	24.1	0.75	534	298	0.05390	3.6	0.3881	4.0	0.05223	1.6	328.2	5.1	367.0	82	314.3	10.6
16YN-03 Rhyolite																
03-2	7.2	0.78	171	90	0.05160	6.7	0.3453	6.9	0.04853	1.7	305.5	5.1	267.9	154	310.5	17.3
03-3	16.9	0.29	400	229	0.05399	2.6	0.3658	3.0	0.04915	1.5	309.3	4.6	370.5	57	316.3	7.7
03-4	44.7	0.30	667	481	0.05852	4.0	0.6282	4.3	0.07785	1.5	483.3	7.2	549.4	88	486.0	15.0
03-5	53.7	0.03	1241	999	0.05291	1.1	0.3670	1.7	0.05031	1.4	316.4	4.3	325.0	24	324.9	5.0
03-6	22.7	0.22	533	393	0.05269	2.3	0.3587	2.7	0.04937	1.4	310.7	4.4	315.5	52	309.5	6.4
03-7	10.2	0.15	241	117	0.05130	2.2	0.3491	2.7	0.04936	1.6	310.6	4.8	254.3	51	329.8	7.8
03-8	28.3	0.13	669	422	0.05193	1.7	0.3526	2.2	0.04925	1.5	309.9	4.5	282.2	38	308.3	6.0
03-9	26.6	0.15	616	608	0.05238	1.6	0.3627	2.2	0.05022	1.5	315.9	4.6	301.8	37	312.8	6.9
03-10	32.1	0.10	757	822	0.05181	1.6	0.3523	2.2	0.04931	1.5	310.3	4.4	277.0	37	313.0	5.5
03-11	17.0	0.00	403	233	0.05208	1.6	0.3532	2.2	0.04918	1.5	309.5	4.6	289.1	38	314.3	6.2
03-12	19.9	0.24	472	319	0.05281	1.7	0.3574	2.2	0.04908	1.5	308.8	4.5	320.8	38	306.3	5.8
03-14	27.2	0.00	644	522	0.05228	1.4	0.3549	2.1	0.04924	1.5	309.9	4.5	297.5	33	301.4	5.1
03-15	32.5	0.17	771	922	0.05144	1.9	0.3474	2.4	0.04897	1.5	308.2	4.4	260.8	44	306.7	5.2
03-16	20.6	0.11	492	360	0.05249	2.7	0.3531	3.3	0.04879	1.9	307.1	5.7	306.9	60	293.5	6.5
03-17	37.6	0.14	873	544	0.05267	1.2	0.3635	1.9	0.05005	1.5	314.8	4.5	314.4	27	312.4	5.3
03-18	37.8	0.02	817	651	0.05293	1.2	0.3926	1.9	0.05379	1.5	337.7	4.8	326.0	28	344.0	5.7
03-20	17.5	0.66	408	391	0.05386	3.1	0.3671	3.4	0.04943	1.5	311.0	4.6	365.2	69	302.0	6.7

[a] Indicates the radiogenic Pb content.
[b] Indicates the common Pb content, based on the $(^{204}Pb/^{206}Pb)_{measured}/(^{204}Pb/^{206}Pb)_{common}$.

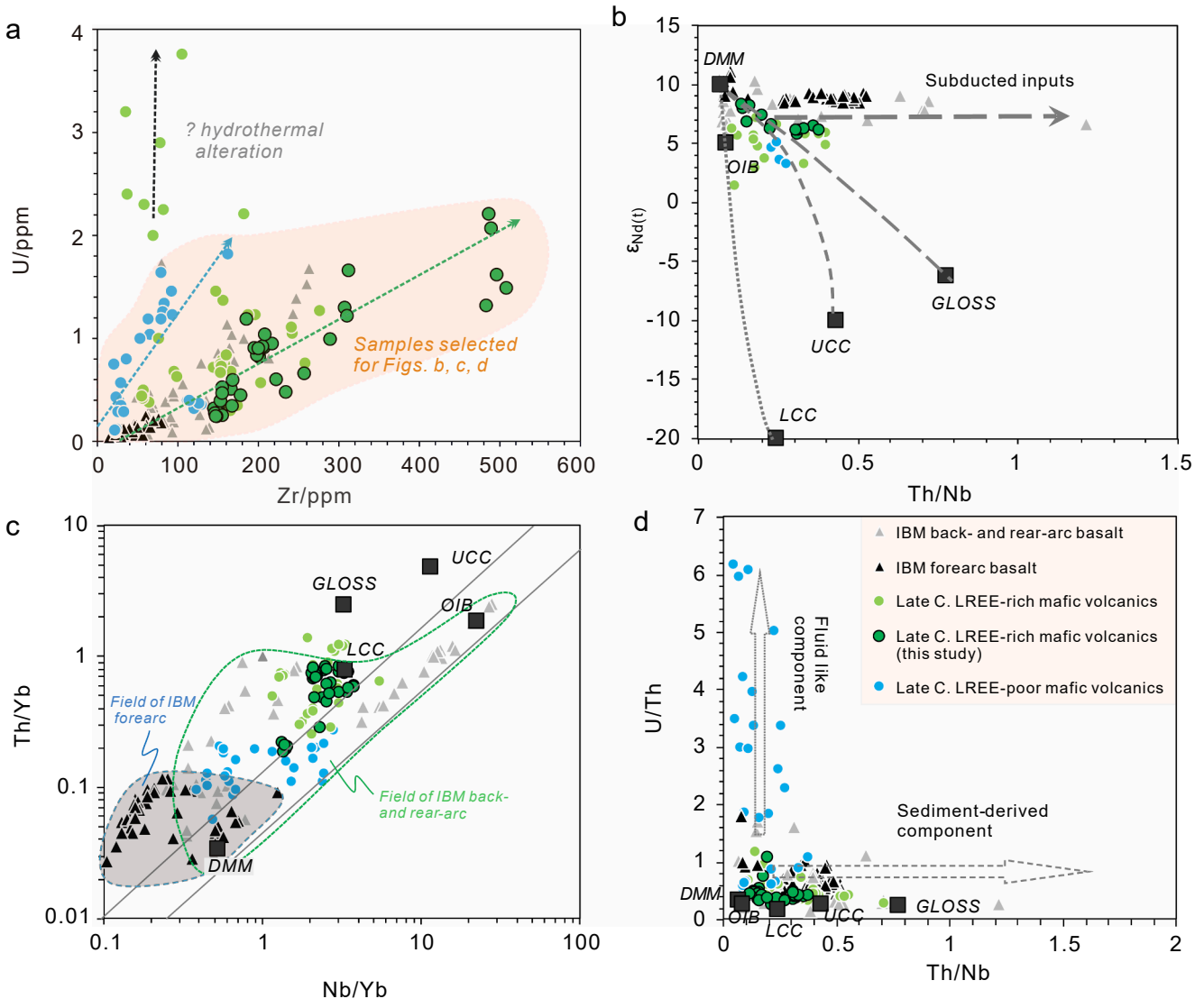

Fig. 9. Plots of (a) U versus Zr, (b) $\varepsilon_{Nd(t)}$ versus Th/Nb, (c) Th/Yb versus Nb/Yb and (d) U/Th versus Th/Nb for Late C. (Carboniferous) mafic volcanics in the Yamansu volcanic arc. The $\varepsilon_{Nd(t)}$ values of DMM, OIB, UCC and LCC are assumed to be +10, +5, −10 and −20, respectively. In Fig. b, the curves represent AFC (assimilation fractional crystallization) of DMM with GLOSS, UCC and LCC after Xie et al. (2016). Data source is the same as in Figs. 7 and 8.

near-primary basalts and still contain very low Nb/La ratios (0.2–0.5) with low Nb contents (2–7 ppm). Regardless of the samples suffering crustal contamination, the LREE-rich mafic volcanics have trace element patterns and ratios (e.g., Nb/Yb and Th/Yb ratios) similar to those of the IBM back- and rear-arc basalts (Figs. 7, 9). The paradox could not be explained by the single role of crustal contamination. Similar to the IBM back- and rear-arc basalts (Fig. 8), a mantle source metasomatized by subducted materials is suggested here. The LREE-rich mafic volcanics have low U/Th (mostly < 1) and high Th/Nb ratios (up to 0.7), suggesting the metasomatism of subducted sediment-derived melts (Fig. 9c). Although they were all from a depleted mantle wedge, the scattered Nd isotopes ($\varepsilon_{Nd(t)}$ = +3.2 to +8.2) of the LREE-rich basalts with MgO > 8% might be attributed to mantle heterogeneity, as they erupted in different areas in the Yamansu volcanic arc (Fig. 8).

5.3. Petrogenesis of the felsic volcanics

Felsic igneous rocks are commonly divided into I-, S-, A-, and M-types according to their different petrogeneses (e.g., Whalen et al., 1987; Chappell, 1999; Frost et al., 2001; Champion and Bultitude, 2013). An M-type origin of the late Carboniferous felsic volcanics in the Yamansu-Kanggur arc could be excluded because M-type granitoids are considered to be generated by fractional crystallization of basaltic magma in a mid-ocean ridge setting, and their occurrence is often accompanied by ophiolite suites. A-type granite is usually characterized by high total alkalis ($Na_2O + K_2O$), FeO_T/MgO and Ga/Al ratios with high HFSE (e.g., Zr, Nb, Ce, Yb, Y), which could be efficiently differentiated from I- and S-type granitoids (Whalen et al., 1987; Chappell and White, 2001; Bonin, 2007). Regardless of some felsic samples with high total alkalis and FeO_T/MgO ratios, all the late Carboniferous rhyolites in the Yamansu volcanic arc plot in the I and S-type fields in the Zr vs. Ga/Al plot (Whalen et al., 1987) and thus argue against an A-type origin (Fig. 10a). The high total alkalis and FeO_T/MgO ratios of some samples might be due to high fractionation with high SiO_2 contents. In addition, following the empirical formula to calculate T_{Zr} (Watson and Harrison, 1983), zircon saturation temperatures (T_{Zr} = 730–830 °C) of the rhyolites are lower than those of A-type grantiods in the Eastern Tianshan (780–908 °C; Zheng et al., 2016; Du et al., 2018). The source rocks of I- and S-type granitoids are generally igneous and sedimentary rocks, respectively. Geochemically, S-type granitoids usually display high A/CNK values (>1.1) relative to I-type granitoids (e.g., Chappell and White, 1992). The P_2O_5 content usually displays a negative relationship

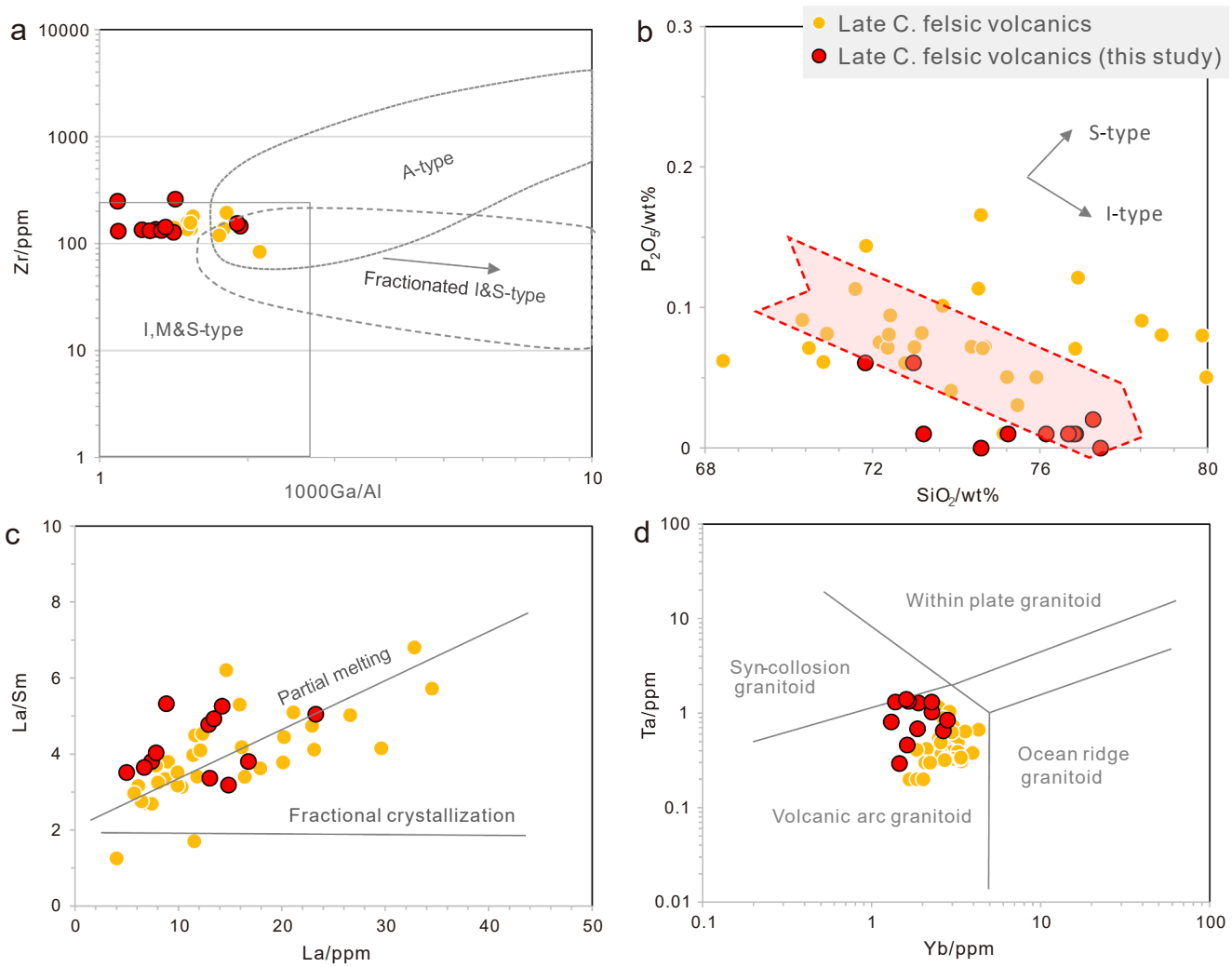

Fig. 10. Classic petrogenetic discrimination diagrams for late C. (Carboniferous) felsic rocks: a) 10000 Ga/Al versus Zr (after Whalen et al., 1987; Wu et al., 2017); b) P_2O_5 versus SiO_2 (after Chappell, 1999); c) La versus La/Sm; d) Yb versus Ta (after Pearce et al., 1984). Previous whole-rock data sources of the late C. volcanics are listed in Appendix S3.

with SiO_2 in I-type granitoids since apatite would be formed prior to crystallization and reduce the P content as the metaluminous magma fractionated (Wolf and London, 1994; Chappell, 1999). In Fig. 10b, the late Carboniferous rhyolites in the Yamansu volcanic arc show an I-type affinity.

Felsic magma can be generated by partial melting of crustal rocks, highly fractional crystallization of mantle-derived mafic magma, or mixing of mantle-derived magma and crust-derived materials (e.g., Clemens et al., 2009; Topuz et al., 2010; Liu et al., 2021). Extremely high SiO_2 (>70%) and low MgO (mostly < 1%) contents of the rhyolites could preclude the magma mixing process. The rhyolites have similar and varying Nd isotopes to the coexistent basaltic magma (Fig. 8a). However, the felsic suites plot along the partial melting curve in Fig. 10c, implying that fractional crystallization played an insignificant role in magma evolution. Additionally, highly fractional crystallization of mafic magma can only produce limited granitic magma (Peccerillo et al., 2003). The absence of large-scale coeval mafic rocks further precludes a considerable effect of fractional crystallization. Thus, the anatexis of crustal igneous rocks is probably the genetic mechanism.

Anatexis modeling requires a hydrated crust or the presence of extra heat (Pin and Paquette, 1997). Extra heat input from magma underplating of their coeval basaltic magma is consistent with variable and high zircon saturation temperatures (T_{Zr} = 730–830 °C) recorded by the late Carboniferous rhyolites. Although it is hard to constrain whether that source protolith is hydrated, based on the existing experiments on anatexis of crustal rocks in both water-poor (Thy et al., 1990) and water-saturated systems (Beard and Lofgren, 1991), plagioclase is always present in residues with magnetite and ilmenite. This inference is consistent with the negative Eu, Sr and Ti anomalies and low Sr/Y ratios of the rhyolites in the Yamansu volcanic arc. Moreover, depletion in Nb and Ta contents might be related to the source rock with arc-like features. Including the analysed rhyolites in this study, the Nd isotopes of the felsic volcanics in the region are scattered from + 6.70 to −0.14 (Fig. 8a). These lines of evidence suggest that the I-type felsic volcanics were likely derived from different source rocks with arc-like features and varied Nd isotopic ratios. Consequently, their calculated one-stage Nd model ages (T_{DM1}) range from 550 to 1150 Ma, inferring that they are generated from Cambrian to Mesoproterozoic arc crustal rocks. In the Eastern Tianshan, only the Central Tianshan seems to have Precambrian basement, and the North and South Tianshan are dominantly built by Paleozoic sedimentary-volcanic strata and magmatic intrusions. Thus, it is likely that the Yamansu volcanic arc was affinal to the Central Tianshan continental arc (Xiao et al., 2004; Charvet et al., 2007).

6. Geodynamic and tectonic implication

As stated above, two different viewpoints for the final closure time of the NTO in the Eastern Tianshan were considered: 1) early

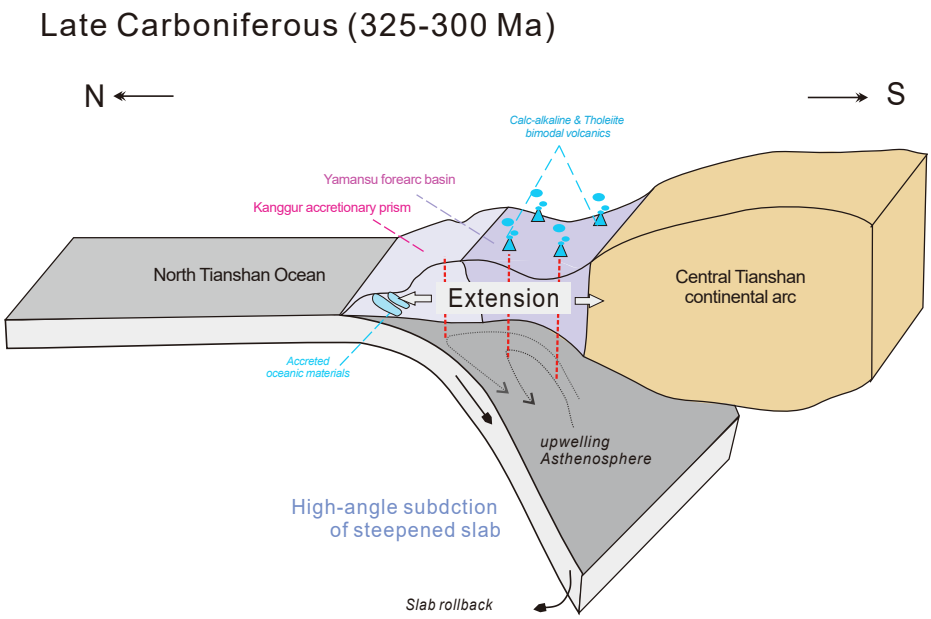

Fig. 11. Schematic tectonic model showing volcanism before closure of the North Tianshan Ocean in the north Central Tianshan forearc system, Eastern Tianshan. See text for details.

Carboniferous (Xia et al., 2004; Wang and Xu, 2006; Yuan et al., 2007; Zhang et al., 2013) or 2) late Carboniferous-early Permian (Ma et al., 1997; Xiao et al., 2004, 2013; Song et al., 2013; Zhang et al., 2016b; Du et al., 2018; Zhao et al., 2018). The variable 494–325 Ma ophiolitic relics discovered in the North Tianshan belt to the west (Fig. 1b), indicate that the NTO opened at least in the early Paleozoic and lasted into the early Carboniferous (e.g., Xu et al., 2006a, 2006b; Li et al., 2008). However, how the North Tianshan ophiolite belt extended eastward is unclear. Ophiolitic mélange outcrops in the Kanggur Fault and composed of serpentinized peridotite, *meta*-gabbro (zircon U–Pb age of 494 ± 10 Ma), *meta*-basalt and chert. Thus, this infers that the North Tianshan Ocean was already in existence during the Cambrian at that place (Li et al., 2008). Additionally, an ophiolitic mélange outcrop without any ages determined was discovered in the Weiya area along the Aqikkuduk Fault and composed of serpentinites, diabases, gabbros, and basalts. Late Devonian sediments unconformably overlie the ophiolitic mélange (Chen et al., 2012). Therefore, it is still not clear when and where the NTO was finally closed by studying the ophiolitic mélanges.

As mentioned above, this study suggests that all the late Carboniferous mafic volcanics in the Yamansu volcanic arc resemble calc-alkaline and tholeiite island arc basaltic series (Figs. 6, 7 and 9), while the late Carboniferous felsic volcanics are akin to I-type arc silicic rocks (Figs. 7, 10). Combined with the extensive occurrence of Carboniferous I-type felsic intrusions in the Yamansu volcanic arc (e.g., Du et al., 2018; Zhao et al., 2018 and references therein), these lines of evidence indicate that it was still an arc setting during the late Carboniferous due to ongoing subduction of the NTO. Furthermore, precise zircon U–Pb ages reported by Song et al. (2021) imply that the magmatic Ni-Cu sulfide mineralized mafic/ultramafic intrusions in the region were emplaced during a short-lived period (290–280 Ma) due to syn- or post-collision between the Dananhu-Bogda and Yamansu-Kanggur arcs. $^{40}Ar/^{39}Ar$ ages of micas- and amphibole-related materials were given from 300 to 230 Ma for activation of the large-scale ductile shear zones along the Kanggur Fault (e.g., Shu et al., 1999; Chen et al., 2005; Wang et al., 2008, 2014). Considering the occurrences of early Permian terrestrial sandstone and conglomerate (Table 1; Zhang et al., 2016b), we suggest the final closure of the NTO and termination of subduction were plausibly prolonged to the boundary of the Carboniferous-Permian (ca. 300 Ma).

According to significant differences in the stratigraphy across the Aqikkuduk Fault together with the occurrence of ophiolitic relics (Chen et al., 2012) and blueschist (Shu et al., 1999), many studies have discussed that the Aqikkuduk Fault was the final suture associated with closure of the NTO (e.g., Song et al., 2013; Wang et al., 2014; Han and Zhao, 2018). However, this model has been challenged by several authors. Specifically, 1) Precambrian inherited zircons are increasingly reported in not only the Carboniferous arc volcanics but also the Devonian-Carboniferous sedimentary rocks of the Yamansu volcanic arc and Kanggur accretionary wedge (Luo et al., 2016; Zhang et al., 2016a; Chen et al., 2019). 2) Ca. 982 Ma quartz arenite cobbles (Chen et al., 2019) and ca. 922 Ma mylonitized granites (Su et al., 2008) were found in the Yamansu volcanic arc, indicating the sporadic occurrence of Proterozoic crust materials. 3) Many Carboniferous volcanics in the Yamansu volcanic arc have very low $\varepsilon_{Nd(t)}$ (close to zero; Fig. 8). 4) The dominant provenance of Devonian-Carboniferous turbiditic sandstones of the Kanggur accretionary wedge was derived from the Central Tianshan arc (Chen et al., 2019). In combination with the northward younger age of the deposition of turbiditic sandstones, these arguments together point to southward subduction with a northward growing accretionary prism (Chen et al., 2019). Therefore, we suggest that the Yamansu volcanic arc and Kanggur accretionary wedge should be the northern part of the Central Tianshan continental arc. The Kanggur Fault with some ophiolite relics (Li et al., 2008) and other ocean mélanges (e.g., N-MORB, E-MORB, pelagic siliceous argillites; Chen et al., 2019) was likely the southernmost suture of the NTO. Compared with the modern Izu-Bonin-Mariana (IBM) arc system (e.g., Taylor and Nesbitt, 1998; Tamura et al., 2005; Ishizuka et al., 2009; Reagan et al., 2010), the late Carboniferous LREE-poor mafic volcanics are similar to the IBM forearc basalts, whereas the LREE-rich mafic suites are akin to the IBM back- and rear-arc basalts (Figs. 8-10). Since the late Carboniferous volcancis with bimodal features covered most of the Yamansu volcanic arc, a forearc extensional basin model is presumably proposed to explain two different arc mafic magmas that occurred in the same volcanic belt.

Consequently, based on several lines of evidence above, we envisage a tectonic model before the closure of the NTO along the Yamansu volcanic arc and Kanggur accretionary wedge (Fig. 11). During the late Carboniferous, bimodal arc volcanics were formed in the Yamansu volcanic arc (Fig. 1c), whereas no coeval volcanics were found in the Central Tianshan arc where the youngest Paleozoic arc volcanics were formed at ca. 347.5 Ma (Mao et al., 2014). This infers that the southward

subducting slab presumably steepened with a large angle in this period to induce extension of arc crust above the subduction zone. Subsequently, the asthenosphere upwelled under the Yamansu arc crust and caused partial melting of the mantle wedge to generate variable calc-alkaline and tholeiite basaltic magmas. As underplating of the mafic magma, I-type felsic magma could be formed by the anatexis of the Yamansu arc crust above where late Carboniferous felsic volcanics with these characteristics erupted extensively.

7. Conclusions

The new data and interpretations lead to the following conclusions: 1) Precise SHRIMP zircon U–Pb ages suggest that the previously identified "Permian" volcanics from the Aqikebulake Formation erupted during the late Carboniferous (318–311 Ma) instead. They are composed of a bimodal calc-alkaline arc lava. 2) Two different varieties of the late Carboniferous mafic volcanics are identified (LREE-poor basalts and LREE-rich basalt–andesites) in the region. The LREE-poor variety with a forearc features was generated from a moderately depleted mantle wedge metasomatized by a subducted fluid-like component. In contrast, the LREE-rich suite should be from a depleted mantle wedge metasomatized by subducted sediment-derived melts. 3) The late Carboniferous rhyolites show an I-type affinity and were derived from anatexis of Cambrian to Mesoproterozoic arc crustal rocks. 4) The Kanggur Fault might be the southernmost suture of the NTO. The Yamanu volcanic arc was a forearc system of the Central Tianshan continental arc due to southward subduction of the NTO.

CRediT authorship contribution statement

Wei Xie: Conceptualization, Validation, Formal analysis, Investigation, Data curation, Writing – original draft, Project administration, Funding acquisition. **Yin Lu:** Validation, Investigation, Formal analysis, Data curation. **Xie-Yan Song:** Conceptualization, Writing – review & editing, Supervision, Project administration, Funding acquisition. **Yu-Feng Deng:** Conceptualization, Investigation, Supervision. **Qing-Lin Liang:** Validation, Investigation, Data curation. **Jun-Nian Yi:** Validation, Investigation, Data curation.

Declaration of Competing Interest

The authors declare that they have no known competing financial interests or personal relationships that could have appeared to influence the work reported in this paper.

Acknowledgements

This study was financially supported by funds from NSFC research grants (41630316, 41873031) and Key Special Project for Introduced Talents Team of Southern Marine Science and Engineering Guangdong Laboratory (Guangzhou) (GML2019ZD0202). Hang-Qiang Xie at the Beijing SHRIMP Centre (National Science and Technology Infrastructure) is thanked for help with technical assistance. We thank Guangqian Hu, Jinlong Ma, Jing Hu, and Jin-Jin Zhu for technical help with diverse solution analyses. The quality of this manuscript was greatly improved by the constructive comments from Dr. Tong Hou and the other two anonymous reviewers, and the editor, Ibrahim Uysal.

Appendix A. Supplementary material

Supplementary data to this article can be found online at https://doi.org/10.1016/j.jseaes.2022.105090.

References

Beard, J.S., Lofgren, G.E., 1991. Dehydration melting and water-saturated melting of basaltic and andesitic greenstones and amphibolites at 1, 3 and 6.9 kb. J. Petrol. 32 (2), 365–401.

BGMRXUAR (Bureau of Geology and Mineral Resources of Xinjiang Uygur Autonomous Region), 1993. Regional Geology of Xinjiang Autonomous Region, Geological Memoirs, No. 32, Map Scale 1:500000. Geological Publishing House, Beijing (in Chinese).

Black, L.P., Kamo, S.L., Allen, C.M., Davis, D.W., Aleinikoff, J.N., Valley, J.W., Mundil, R., Campbell, I.H., Korsch, R.J., Williams, I.S., Foudoulis, C., 2004. Improved 206Pb/238U microprobe geochronology by the monitoring of a trace-element-related matrix effect; SHRIMP, ID-TIMS, ELA-ICP–MS and oxygen isotope documentation for a series of zircon standards. Chem. Geol. 205 (1-2), 115–140.

Bonin, B., 2007. A-type granites and related rocks: Evolution of a concept, problems and prospects. Lithos 97 (1-2), 1–29.

Champion, D.C., Bultitude, R.J., 2013. The geochemical and Sr–Nd isotopic characteristics of Paleozoic fractionated S-types granites of North Queensland: Implications for S-type granite petrogenesis. Lithos 162-163, 37–56.

Chappell, B.W., White, A.J.R., 1992. I- and S-type granites in the Lachlan Fold Belt. Trans. Roy. Soc. Edinburgh: Earth Sci. 83, 1–26.

Chappell, B.W., 1999. Aluminum saturation in I- and S-type granites and the characterization of fractionated haplogranites. Lithos 46, 535–551.

Chappell, B.W., White, A.J.R., 2001. Two contrasting granite types: 25 years later. Aust. J. Earth Sci. 48 (4), 489–499.

Charvet, J., Shu, L.S., Laurent-Charvet, S., 2007. Paleozoic structural and geodynamic evolution of eastern Tianshan (NW China): welding of the Tarim and Junggar plates. Episodes 30, 162–186.

Chen, W., Sun, S., Zhang, Y., Xiao, W.-J., Wang, Y.-T., Wang, Q.-L., Jiang, L.-F., Yang, J.-T., 2005. $^{40}Ar/^{39}Ar$ geochronology of the Qiugemingtashi-Huangshan ducile shear zone in East Tianshan, Xinjiang, NW China. Acta Geol. Sinica 79, 790–804 in Chinese with English abstract.

Chen, X.J., Shu, L.S., Ma, X.X., 2012. Geochemical features and tectonic significances of Weiya ophiolitic mélange and mafic granulite, Xinjiang. Geol. J. China Universities 18, 661–675 in Chinese with English abstract.

Chen, Z., Xiao, W., Windley, B.F., Schulmann, K., Mao, Q., Zhang, Z., Zhang, Ji'en, Deng, C., Song, S., 2019. Composition, provenance, and tectonic setting of the southern Kangurtag accretionary complex in the eastern Tianshan, NW China: implications for the late Paleozoic evolution of the North Tianshan Ocean. Tectonics 38 (8), 2779–2802.

Clemens, J.D., Darbyshire, D.P.F., Flinders, J., 2009. Sources of post-orogenic calc-alkaline magmas: the Arrochar and Garabal Hill-Glen Fyne complexes, Scotland. Lithos 112 (3-4), 524–542.

Compston, W., Williams, I.S., Kirschvink, J.L., Zichao, Zhang, Guogan, M.A., 1992. Zircon U-Pb ages for the early Cambrian timescale. J. Geol. Soc., London 149 (2), 171–184.

Cui, C., Yu, J.J., Yang, W.Z., Zhang, Y.H., Cui, Y.C., Yu, J.L., 2018. Geochronology, geochemistry and genesis of Yamansu Formation volcanic rocks of southern Aqi Mountain in Jueluotage tectonic belt, eastern Tianshan of Xinjiang. Global Geol. 37, 88–104 in Chinese with English abstract.

Du, L., Long, X., Yuan, C., Zhang, Y., Huang, Z., Wang, X., Yang, Y., 2018. Mantle contribution and tectonic transition in the Aqishan-Yamansu Belt, Eastern Tianshan, NW China: Insights from geochronology and geochemistry of Early Carboniferous to Early Permian felsic intrusions. Lithos 304-307, 230–244.

Elliott, T., Plank, T., Zindler, A., White, W., Bourdon, B., 1997. Element transport from slab to volcanic front at the Mariana arc. J. Geophys. Res. 102 (B7), 14991–15019.

Frost, B.R., Barnes, C.G., Collins, W.J., Arculus, R.J., Ellis, D.J., Frost, C.D., 2001. A geochemical classification for granitic rocks. J. Petrol. 42, 2033–2048.

Han, Y., Zhao, G., 2018. Final amalgamation of the Tianshan and Junggar orogenic collage in the southwestern Central Asian Orogenic Belt: constraints on the closure of the Paleo-Asian Ocean. Earth Sci. Rev. 186, 129–152.

Hawkesworth, C., Turner, S., Peate, D., McDermott, F., van Calsteren, P., 1997. Elemental U and Th variations in island arc rocks: implications for U-series isotopes. Chem. Geol. 139 (1-4), 207–221.

Hou, T., Zhang, Z., Santosh, M., Encarnacion, J., Zhu, J., Luo, W., 2014. Geochronology and geochemistry of submarine volcanic rocks in the yamansu iron deposit, eastern Tianshan Mountains, NW China: Constraints on the metallogenesis. Ore Geol. Rev. 56, 487–502.

Huang, X., Zhang, X., Wang, Y., Wang, X., Luan, T., Lin, W., Wang, Q., Hu, K., 2021. Integrated biostratigraphy and age assignment for Carboniferous successions in the Qoltag tectonic belt in eastern Tianshan, NW China. J. Asian Earth Sci. 207, 104630. https://doi.org/10.1016/j.jseaes.2020.104630.

Irvine, T.N., Baragar, W.R.A., 1971. A guide to the chemical classification of the common volcanic rocks. Can. J. Earth Sci. 8 (5), 523–548.

Ishizuka, O., Yuasa, M., Taylor, R.N., Sakamoto, I., 2009. Two contrasting magmatic types coexist after the cessation of back-arc spreading. Chem. Geol. 266 (3-4), 274–296.

Jiang, H., Han, J., Chen, H., Zheng, Y.i., Lu, W., Deng, G., Tan, Z., 2017. Intra-continental back-arc basin inversion and late Carboniferous magmatism in Eastern Tianshan, NW China: Constraints from the Shaquanzi magmatic suite. Geosci. Front. 8 (6), 1447–1467.

Le Maitre, R.W., 1989. A Classification of Igneous Rocks and Glossary Terms: recommendations of the International Union of Geological Sciences Subcommission on the Systematics of Igneous Rocks. Blackwell Scientific Publications, Trowbridge, Wilts, UK, pp. 1–193.

Li, W.Q., Ma, H.D., Wang, R., Wang, H., Xia, B., 2008. SHRIMP dating and Nd-Sr isotopic tracing of Kanggurtage ophiolite in eastern Tianshan, Xinjiang. Acta Petrol. Sinica 4, 773–780 in Chinese with English abstract.
Li, X.-H., Li, Z.-X., Wingate, M.T.D., Chung, S.-L., Liu, Y., Lin, G.-C., Li, W.-X., 2006. Geochemistry of the 755 Ma Mundine well dyke swarm, Northwestern Australia: part of a Neoproterozoic mantle superplume beneath Rodinia? Precambr. Res. 146 (1-2), 1–15.
Li, Y., Yang, J.S., Zhang, J., Li, T.F., Chen, S.Y., Ren, Y.F., Xu, X.Z., 2011. Tectonical significance of the Carboniferous volcanic rocks in estern Tianshan. Acta Petrol. Sinica 27, 193–209 in Chinese with English abstract.
Liu, B., Wu, J.-H., Li, H., Mathur, R., Wu, Q.-H., Zheng, H., Jiang, J.-B., 2021. Late Paleozoic tectonic evolution of the Kangguer Shear Zone and Yamansu Arc Belt, Eastern Tianshan (NW China): constraints from structure, petrogenesis and geochronology of granitoids. Lithos 380-381, 105821. https://doi.org/10.1016/j.lithos.2020.105821.
Ludwig, K.R., 2001. SQUID 1.02, A User's Manual, Berkeley Geochronology Center Special Publication No.2. p. 17.
Ludwig, K.R., 2003. Isoplot 3.0: A Geochronological Toolkit for Microsoft Excel. Berkeley Geochronol. Centre, Spec. Publ. 4, 1–70.
Luo, T., Liao, Q.-A., Chen, J.-P., Zhang, X.-H., Guo, D.-B., Hu, Z.-C., 2012. LA-ICP–MS zircon U-Pb dating of the volcanic rocks from Yamansu Formation in the Eastern Tianshan, and its geological signifcance. Earth Sci.-J. China Univ. Geosci. 37, 1338–1352 in Chinese with English abstract.
Luo, T., Liao, Q.-A., Zhang, X.-H., Chen, J.-P., Wang, G.-C., Huang, X., 2016. Geochronology and geochemistry of Carboniferous metabasalts in eastern Tianshan, Central Asia: evidence of a back-arc basin. Int. Geol. Rev. 58 (6), 756–772.
Ma, R.S., Shu, L.S., Sun, J.Q., 1997. Tectonic Evolution and Metallization in the eastern Tianshan Belt, China. Geological Publish House, Beijing, p. 202 (in Chinese with English abstract).
Mao, Q., Wang, J., Xiao, W., Fang, T., Wang, N., Yu, M., 2014. The discovery of Low-Carboniferous arc volcanic rocks and its tectonic signifance at the Kalatage area in the Central Tianshan, Eastern Tianshan Mountains, Xinjiang, NW China. Acta Geol. Sin. 88, 1790–1799 in Chinese with English abstract.
McDonough, W.F., Sun, S.-s., 1995. The composition of the Earth. Chem. Geol. 120 (3-4), 223–253.
Pearce, J.A., Harris, N.B.W., Tindle, A.G., 1984. Trace-element discrimination diagrams for the tectonic interpretation of granitic-rocks. J. Petrol. 25 (4), 956–983.
Peccerillo, A., Barberio, M.R., Yirgu, G., Ayalew, M., Barbieri, D., Wu, T.W., 2003. Relationships between mafic and peralkaline silicic magmatism in continental rift settings: a petrological, geochemical and isotopic study of the Gedemsa Volcano, central Ethiopian rift. J. Petrol. 44, 2003–2032.
Pin, C., Paquette, J.L., 1997. A mantle-derived bimodal suite in the Hercynian Belt: Nd isotope and trace element evidence for a subduction-related rift origin of the Late Devonian BreÂvenne metavolcanics, Massif Central (France). Contrib. Miner. Petrol. 129, 222–238.
Plank, T., Langmuir, C.H., 1998. The chemical composition of subducting sediment and its consequences for the crust and mantle. Chem. Geol. 145 (3-4), 325–394.
Qi, L., Hu, J., Conrad, G., 2000. Determination of trace elements in granites by inductively coupled plasma mass spectrometry. Talanta 51, 507–513.
Reagan, M.K., Ishizuka, O., Stern, R.J., Kelley, K.A., Ohara, Y., Blichert-Toft, J., Bloomer, S.H., Cash, J., Fryer, P., Hanan, B.B., Hickey-Vargas, R., Ishii, T., Kimura, J.-I., Peate, D.W., Rowe, M.C., Woods, M., 2010. Fore-arc basalts and subduction initiation in the Izu–Bonin–Mariana system. Geochem. Geophys. Geosyst. 11 (3), n/a–n/a. https://doi.org/10.1029/2009GC002871.
Rudnick, R.L., Gao, S., 2003. Composition of the continental crust. In: Rudnick, R.L. (Ed.), Treatise on Geochemistry. Elsevier, Amsterdam, pp. 1–64.
Şengör, A.M.C., Natal'in, B.A., Burtman, V.S., 1993. Evolution of the Altaid tectonic collage and Palaeozoic crustal growth in Eurasia. Nature 364 (6435), 299–307.
Shu, L.S., Charvet, J., Guo, L.Z., Lu, H.F., Laurent-Charvet, S., 1999. A large-scale Palaeozoic dextral ductile strike-slip zone: the Aqqikkudug-Weiya zone along the northern margin of the Central Tianshan belt, Xinjiang, NW China. Acta Geol. Sinica 73 (2), 148–162.
Singer, B.S., Jicha, B.R., Leeman, W.P., Rogers, N.W., Thirlwall, M.F., Ryan, J., Nicolaysen, K.E., 2007. Along-strike trace element and isotopic variation in Aleutian Island Arc basalt: subduction melts sediments and dehydrates serpentine. J. Geophys. Res. 112, B06206. https://doi.org/10.1029/2006JB004897.
Song, X.-Y., Chen, L.-M., Deng, Y.-F., Xie, W., 2013. Syn-collisional tholeiitic magmatism induced by asthenosphere upwelling due to slab detachment at the southern margin of the Central Asian Orogenic Belt. J. Geol. Soc., London 170, 941–950.
Song, X.-Y., Deng, Y.-F., Xie, W., Yi, J.-N., Fu, B., Chen, L.-M., Yu, S.-Y., Zheng, W.-Q., Liang, Q.-L., 2021. Prolonged basaltic magmatism and short-lived magmatic sulfide mineralization in orogenic belts. Lithos 390-391, 106114. https://doi.org/10.1016/j.lithos.2021.106114.
Stacey, J.S., Kramers, J.D., 1975. Approximation of Terrestrial Lead Isotope Evolution by a Two-Stage Model. Earth Planet. Sci. Lett. 26 (2), 207–221.
Stracke, A., 2012. Earth's heterogeneous mantle: a product of convection-driven interaction between crust and mantle. Chem. Geol. 330-331, 274–299.
Su, C.Q., Jiang, C.Y., Xia, M.Z., Zhang, L., Ji, H.G., Guo, F.F., Liu, X.J., 2008. Zircon SHRIMP U-Pb dating from granite of the metamorphic core complex system in Jueluotage tectonic belt and its geological significance. Acta Petrologica Sinica 24, 2789–2799 in Chinese with English abstract.
Su, C.Q., Jiang, C.Y., Xia, M.Z., Wei, W., Pan, R., 2009. Geochemistry and zircons SHRIMP U-Pb age of volcanic rocks of Aqishan Formation in the eastern area of north Tianshan, China. Acta Petrologica Sinica 25, 901–915 in Chinese with English abstract.
Tamura, Y., Tani, K., Ishizuka, O., Chang, Q., Shukuno, H., Fiske, R.S., 2005. Are arc basalts dry, wet, or both? Evidence from the Sumisu caldera volcano, Izu–Bonin arc, Japan. J. Petrol. 46, 1769–1803.
Taylor, R.N., Nesbitt, R.W., 1998. Isotopic characteristics of subduction fluids in an intraoceanic setting, Izu-Bonin Arc, Japan. Earth Planet. Sci. Lett. 164 (1-2), 79–98.
Thy, P., Beard, J.S., Lofgred, G., 1990. Experimental constraints on the origin of Icelandic rhyolites. J. Geol. 98, 417–421.
Topuz, G., Altherr, R., Siebel, W., Schwarz, W.H., Zack, T., Hasözbek, A., Barth, M., Satır, M., Şen, C., 2010. Carboniferous high-potassium I-type granitoid magmatism in the Eastern Pontides: the Gümüşhane pluton (NE Turkey). Lithos 116 (1-2), 92–110.
Wang, B., Cluzel, D., Jahn, B.-m., Shu, L., Chen, Y., Zhai, Y., Branquet, Y., Barbanson, L., Sizaret, S., 2014. Late Paleozoic pre- and syn-kinematic plutons of the Kangguer-Huangshan Shear zone: inference on the tectonic evolution of the eastern Chinese north Tianshan. Am. J. Sci. 314 (1), 43–79.
Wang, J.B., Xu, X., 2006. Post-collisional tectonic evolution and metallogenesis in Northern Xinjiang, China. Acta Geol. Sinica 80, 23–31 in Chinese with English abstract.
Wang, Y.u., Li, J., Sun, G., 2008. Postcollisional eastward extrusion and tectonic exhumation along the eastern Tianshan Orogen, Central Asia: constraints from dextral strike-slip motion and $^{40}Ar/^{39}Ar$ geochronological evidence. J. Geol. 116 (6), 599–618.
Watson, E.B., Harrison, T.M., 1983. Zircon saturation revisited: temperature and composition effects in a variety of crustal magma types. Earth Planet. Sci. Lett. 64 (2), 295–304.
Whalen, J.B., Currie, K.L., Chappell, B.W., 1987. A-type granites: geochemical characteristics, discrimination and petrogenesis. Contrib. Miner. Petrol. 95 (4), 407–419.
Williams, I.S., 1998. U-Th-Pb geochronology by ion microprobe. Rev. Econ. Geol. 7, 1–35.
Winchester, J.A., Floyd, P.A., 1977. Geochemical discrimination of different magma series and their differentiation products using immobile elements. Chem. Geol. 20, 325–343.
Windley, B.F., Alexeiev, D., Xiao, W., Kröner, A., Badarch, G., 2007. Tectonic models for accretion of the Central Orogenic Belt. J. Geol. Soc., London 164, 31–47.
Wolf, M.B., London, D., 1994. Apatite dissolution into peraluminous haplogranitic melts: an experimental study of solubilities and mechanisms. Geochim. Cosmochim. Acta 58 (19), 4127–4145.
Wu, FuYuan, Liu, XiaoChi, Ji, WeiQiang, Wang, JiaMin, Yang, L., 2017. Highly fractionated granites: recognition and research. Sci. China Earth Sci. 60 (7), 1201–1219.
Xia, L.-Q., Xia, Z.-C., Xu, X.-Y., Li, X.-M., Ma, Z.-P., Wang, L.-S., 2004. Carboniferous Tianshan igneous megaprovince and mantle plume. Geol. Bull. China 23, 903–910 in Chinese with English abstract.
Xiao, W.-J., Zhang, L.-C., Qin, K.-Z., Sun, S., Li, J.-L., 2004. Paleozoic accretionary and collisional tectonics of the Eastern Tianshan (China): implications for the continental growth of Central Asia. Am. J. Sci. 304, 370–395.
Xiao, W., Windley, B.F., Allen, M.B., Han, C., 2013. Paleozoic multiple accretionary and collisional tectonics of the Chinese Tianshan orogenic collage. Gondwana Res. 23 (4), 1316–1341.
Xie, W., Xu, Y.-G., Chen, Y.-B., Luo, Z.-Y., Hong, L.-B., Ma, L., Liu, H.-Q., 2016. High–alumina basalts from the Bogda Mountains suggest an arc setting for Chinese Northern Tianshan during the Late Carboniferous. Lithos 256-257, 165–181.
Xu, L., Chai, F., Li, Q., Zeng, H., Geng, X., Xia, F., Deng, G., 2014. Geochemistry and zircon U-Pb age of volcanic rocks from the Shaquanzi Fe-Cu deposit in East Tianshan Mountains and their geological significance. Geol. China 41, 1771–1790 in Chinese with English abstract.
Xu, X., Li, X., Ma, Z., Xia, L., Xia, Z., Pen, G., 2006a. LA-ICPMS zircon U-Pb dating of gabbro from the Bayingou ophiolite in the northern Tianshan Mountains. Acta Geol. Sin. 80, 1168–1176 in Chinese with English abstract.
Xu, X., Xia, L., Ma, Z., Wang, Y., Xia, Z., Li, X., Wang, L., 2006b. SHRIMP zircon U-Pb geochronology of the plagiogranites from Bayingou ophiolite in North Tianshan Mountains and the petrogenesis of the ophiolite. Acta Petrol. Sinica 22, 83–94 in Chinese with English abstract.
Yuan, F., Zhou, T.F., Fan, Y., Tan, L.G., David, C., Sebastien, M., Wang, Q.M., Wang, W.J., 2007. LA-ICPMS U-Pb age of zircon from basalt of Matoutan Group in Shilipo native copper mineralized area, Eastern Tianshan, Xinjiang. Acta Petrol. Sinica 23, 1973–1980 in Chinese with English abstract.
Zhang, D.Y., Zhou, T.F., Yuan, F., Liu, S., Lu, Y.J., Xu, C., Ning, F.Q., 2012a. Geochronology and geological indication of the native copper mineralized basalt formation in Jueluotage area, Eastern Tianshan, Xinjiang. Acta Petrol. Sinica 28, 2392–2400 in Chinese with English abstract.
Zhang, X., Huang, X., Chen, J., Liao, Q., Duan, X., 2012b. Stratigraphical sequence of Carboniferous marine volcanic-deposit rock and its geological age in Jueluotage area, Eastern Tianshan. Earth Sci.-J. China Univ. Geosci. 37, 1305–1314 in Chinese with English abstract.
Zhang, D., Zhou, T., Yuan, F., Fiorentini, M.L., Said, N., Lu, Y., Pirajno, F., 2013. Geochemical and isotopic constraints on the genesis of the Jueluotage native copper mineralized basalt, Eastern Tianshan, Northwest China. J. Asian Earth Sci. 73, 317–333.
Zhang, W., Chen, H., Han, J., Zhao, L., Huang, J., Yang, J., Yan, X., 2016a. Geochronology and geochemistry of igneous rocks in the Bailingshan area: Implications for the tectonic setting of late Paleozoic magmatism and iron skarn mineralization in the eastern Tianshan, NW China. Gondwana Res. 38, 40–59.
Zhang, X., Zhao, G., Sun, M., Eizenhöfer, P.R., Han, Y., Hou, W., Liu, D., Wang, B.o., Liu, Q., Xu, B., 2016b. Tectonic evolution from subduction to arc-continent collision

of the Junggar ocean: constraints from U-Pb dating and Hf isotopes of detrital zircons from the North Tianshan belt, NW China. Geol. Soc. Am. Bull. 128 (3-4), 644–660.
Zhang, Y., Sun, M., Yuan, C., Long, X., Jiang, Y., Li, P., Huang, Z., Du, L., 2018. Alternating trench advance and retreat: Insights from Paleozoic magmatism in the eastern Tianshan, Central Asian Orogenic Belt. Tectonics 37 (7), 2142–2164.
Zhang, S., Chen, H., Hollings, P., Zhao, L., Gong, L., 2020. Tectonic and magmatic evolution of the Aqishan-Yamansu belt: A Paleozoic arc-related basin in the Eastern Tianshan (NW China). Geol. Soc. Am. Bull. 133, 1320–1344.
Zhao, L., Chen, H., Zhang, L.i., Zhang, W., Yang, J., Yan, X., 2018. The Late Paleozoic magmatic evolution of the Aqishan-Yamansu belt, Eastern Tianshan: Constraints from geochronology, geochemistry and Sr–Nd–Pb–Hf isotopes of igneous rocks. J. Asian Earth Sci. 153, 170–192.
Zhao, L., Chen, H., Hollings, P., Han, J., 2019. Tectonic transition in the Aqishan-Yamansu belt, Eastern Tianshan: constraints from the geochronology and geochemistry of Carboniferous and Triassic igneous rocks. Lithos 344-345, 247–264.
Zheng, J., Mao, J., Chai, F., Yang, F., 2016. Petrogenesis of Permian A-type granitoids in the Cihai iron ore district, Eastern Tianshan, NW China: Constraints on the timing of iron mineralization and implications for a non-plume tectonic setting. Lithos 260, 371–383.